J. Fluid Mech. (2010), *vol.* 656, *pp.* 51–81. © Cambridge University Press 2010
doi:10.1017/S0022112010001023

Dissipative small-scale actuation of a turbulent shear layer

B. VUKASINOVIC[1]†, Z. RUSAK[2] AND A. GLEZER[1]

[1]Woodruff School of Mechanical Engineering, Georgia Institute of Technology, Atlanta, GA 30332-0405, USA

[2]Department of Mechanical, Aerospace and Nuclear Engineering, Rensselaer Polytechnic Institute, Troy, NY 12180-3590, USA

(Received 11 August 2008; revised 22 February 2010; accepted 23 February 2010; first published online 2 June 2010)

The effects of small-scale dissipative fluidic actuation on the evolution of large- and small-scale motions in a turbulent shear layer downstream of a backward-facing step are investigated experimentally. Actuation is applied by modulation of the vorticity flux into the shear layer at frequencies that are substantially higher than the frequencies that are typically amplified in the near field, and has a profound effect on the evolution of the vortical structures within the layer. Specifically, there is a strong broadband increase in the energy of the small-scale motions and a nearly uniform decrease in the energy of the large-scale motions which correspond to the most amplified unstable modes of the base flow. The near field of the forced shear layer has three distinct domains. The first domain ($x/\theta_0 < 50$) is dominated by significant concomitant increases in the production and dissipation of turbulent kinetic energy and in the shear layer cross-stream width. In the second domain ($50 < x/\theta_0 < 300$), the streamwise rates of change of these quantities become similar to the corresponding rates in the unforced flow although their magnitudes are substantially different. Finally, in the third domain ($x/\theta_0 > 350$) the inviscid instability of the shear layer re-emerges in what might be described as a 'new' baseline flow.

1. Introduction

The flow dynamics of shear layers has a profound effect on system performance in a number of practical applications including aerodynamic forces and moments, optical transmission, acoustic noise, combustion efficiency and emissions and thermal signature. It is well known that the evolution of these shear flows is largely dominated by a hierarchy of vortical structures of decreasing scales which evolve as a result of inherent hydrodynamic instabilities of the base flow (e.g. Brown & Roshko 1974; Winant & Browand 1974; Ho & Huerre 1984). The susceptibility of the shear layer to controlled excitation within the receptivity range of its unstable modes has led to a number of attempts to manipulate the evolution of the primary (large-scale) vortices and thereby affect global flow characteristics (e.g. mitigation of separation, Greenblatt & Wygnanski 2000; mixing of species in non-reacting and reacting flows, Gutmark, Schadow & Yu 1995; and suppression of unsteady aerodynamic loads, Cattafesta *et al.* 2008; etc.). In some cases the flow manipulation can be complicated or even dominated by coupling to feedback from other instabilities of the base flow

† Email address for correspondence: bojan.vukasinovic@me.gatech.edu

https://doi.org/10.1017/S0022112010001023 Published online by Cambridge University Press

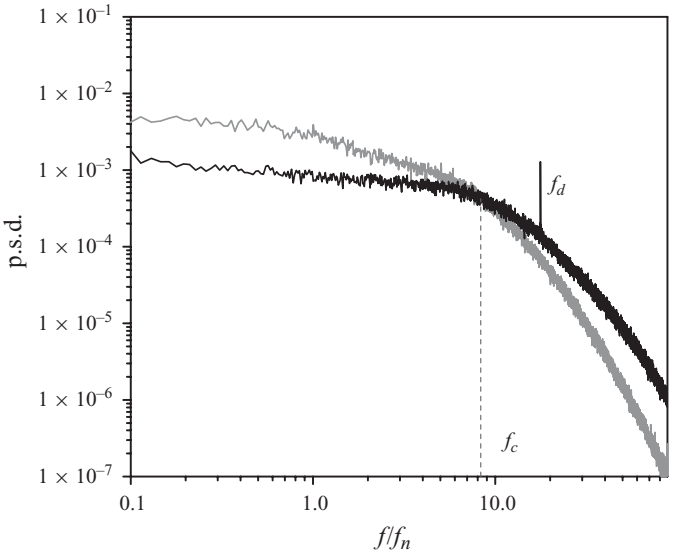


FIGURE 1. Power spectra of velocity fluctuations measured in the near field of a plane shear layer illustrating the effects of direct small-scale actuation at $f_d \gg f_n$ (f_n is the 'natural' frequency). The actuation results in a concomitant decrease in the energy of the large-scale ($f < f_c$) motions, and increase in energy of the small-scale ($f > f_c$) motions.

such as cavity modes (Rockwell & Naudascher 1978), the near wake of stalled airfoils (Wu *et al.* 1998) and vortex formation in the wake of bluff bodies (Unal & Rockwell 1988). A clear risk in excitation at or near globally unstable frequencies has been the undesired amplification of 'spurious' unsteady modes as demonstrated by the cavity experiments of Debiasi & Samimy (2003).

A different approach for modification of the flow characteristics that are associated with the presence of the large-scale vortical structures is to affect their formation and evolution by altering the base flow instabilities that lead to their formation. This is accomplished using direct small-scale ('dissipative') actuation having characteristic wavelengths that are typically an order of magnitude smaller than the relevant local or global length scale of the base flow. This approach, which was demonstrated by Wiltse & Glezer (1993), emphasizes actuation frequencies that are high enough so that they are effectively 'decoupled' from the unstable frequencies of the base flow and the effects are therefore frequency-independent (below some practical upper limit).

Figure 1 shows velocity power spectra that are measured in the near field of a single-stream plane shear layer for the base flow and in the presence of actuation at frequency f_d which is deliberately applied within the dissipation range of the (unforced) flow. The actuation frequency is nominally an order of magnitude higher than the most unstable 'natural' frequency f_n, which is often referred to (based on the linear stability analysis) as the 'most amplified' frequency and is associated with the peak spectral components of the velocity field. An important feature of the spectra in figure 1 is the change in the magnitudes of spectral components above and below their 'crossover' frequency f_c. In the forced flow, spectral components of the 'large scales' below f_c are significantly attenuated while the spectral components of the 'small scales' above f_c are significantly enhanced. These effects indicate that direct actuation at the small scales can lead to an acceleration of the energy cascade from the large- to small-scale motions within the flow. Wiltse & Glezer (1998) also showed that the

https://doi.org/10.1017/S0022112010001023 Published online by Cambridge University Press

actuation results in the suppression of 'natural' instability modes in the baseline flow and that the direct addition of high-frequency energy into the shear layer alters the energy cascade across a broadband range. They further postulated that enhanced energy transfer from large to small scales may be the driving mechanism.

The effectiveness of this actuation approach has been demonstrated in several investigations of the suppression of separation over a broad range of St_{act}, including the works of Erk (1997, $St_{act} \approx 100$), Glezer, Amitay & Honohan (2005, $St_{act} \approx 10$), Vukasinovic & Glezer (2007, $St_{act} \approx 15$) and Ben-Hamou, Arad & Seifert (2007, $St_{act} = 18$–55). These investigators showed that even though the actuation is introduced at scales that are typically smaller than the naturally dominant scales of the base flow, it effectively decouples the evolution of the shear layer from the wake instability and perhaps suppresses the inherent low-frequency feedback (e.g. in cavity flows, Rockwell & Naudascher 1978). Such bypass of the internal flow feedback was demonstrated by reduction of cavity noise and significant flow stabilization (Stanek *et al.* 2000; Arunajatesan, Shipman & Sinha 2002) and in the suppression of vortical structures in a single-stream shear layer that was deliberately forced within its receptivity range (Vukasinovic & Glezer 2006).

Another example of the effectiveness of this actuation approach has been the mitigation of optical aberrations that occur during the transmission of optical wavefronts through a turbulent shear flow (Bower *et al.* 2004). This approach was demonstrated by Zubair *et al.* (2007) who used high-frequency actuation in a plane shear layer to significantly reduce optical aberrations by suppressing the large-scale vortical motions. The numerical simulations of Visbal & Rizzetta (2008) also show significant reduction in optical aberrations through free and cavity-bound shear layers as a result of the suppression of the large-scale coherence by small-scale actuation. More recently, Oljaca & Glezer (2009) used a small-scale dissipative harmonic excitation in a two-stream shear layer to suppress the baseline 'natural' flow vortices and to enhance small-scale mixing.

It would be expected that the suppression of the coherent large-scale motions in shear flows would ultimately lead to reduced production of turbulent kinetic energy (TKE) and diminution of overall turbulent fluctuations. In fact, these effects were observed in a number of early investigations of forced shear layers. Vlasov & Ginevskii (1973) reported the suppression of velocity fluctuations in the near field of an axisymmetric turbulent jet when acoustic excitation was applied at frequencies that correspond to multiples of a natural jet frequency ($St_D > 2$). Similarly, Rockwell (1972) who studied forced excitation of a plane jet by transverse oscillations identified a 'preservation' regime in which a natural vortex rollup was spatially delayed when the harmonic actuation was applied at a frequency that was about two times higher than the natural frequency. Subsequently, Zaman & Hussain (1981) investigated the suppression of velocity fluctuations in several shear flows using acoustic and mechanical actuation at frequencies up to about twice the 'natural' unstable flow frequencies. They found that the optimal actuation frequency for turbulence suppression was $St_{\theta 0} \cong 0.017$ (based on the initial thickness of the shear layer), which was attributed to spatially compressed rollup and breakdown of the forced flow. In a related investigation, Hussain & Hasan (1985) showed that this turbulence suppression led to the reduction of the broadband far-field jet noise. The study of Nallasamy & Hussain (1989) in a shear layer of an axisymmetric jet showed that the maximum turbulence suppression depends on both the actuation amplitude and frequency. In a later study, Zaman & Rice (1992) conjectured that the suppression could result from inhibition of vortex pairing, decoupling of the

https://doi.org/10.1017/S0022112010001023 Published online by Cambridge University Press

upstream boundary layer instability from the shear layer instability, or 'tripping' of the transitional boundary layer. More recently, Samimy *et al.* (2007) also reported noise suppression in $M = 0.9$ axisymmetric jets, when high-frequency plasma actuation is applied at $St_D > 1.5$, substantially higher than the characteristic frequencies of the natural jet vortices.

A number of investigations have specifically focused on the effects of direct actuation of small-scale (or high-frequency) motions in turbulent shear flows. Wiltse & Glezer (1998) estimated the turbulent dissipation in a jet shear layer that was forced by cantilevered piezoelectric actuators and concluded that even a small increase in the induced displacement perturbations at high actuation frequencies can lead to significant enhancement of dissipation and consequently to a decrease in TKE. Measurements in the near wake of a cylinder where the lift and drag were controlled by small-scale (high-frequency) surface actuation upstream of separation (Honohan, Amitay & Glezer 2000), showed a significant decrease in turbulent stresses in the forced shear layer, suggesting the increased dissipation in the near wake is a result of the forcing. In a numerical study of the effects of high-frequency forcing in a free shear layer, Cain *et al.* (2001) concluded that the reduction in TKE in the forced flow results from simultaneous increase of its dissipation rate and decrease in its production rate. The decrease of turbulent stresses as a result of small-scale actuation was also observed in the wake of an airfoil (Glezer *et al.* 2005) and was attributed to the increased dissipation and a decrease of energy transfer from the free stream. Stanek *et al.* (2002) hypothesized that high-frequency excitation modifies the time-averaged velocity distributions within the baseline shear layer and thereby makes it stable to low-frequency perturbations. This model implies that linear or nonlinear stability analyses can be used to describe high-frequency excitation in a manner similar to what has been used for low-frequency excitation. In a more recent investigation, Stanek *et al.* (2007) emphasized the role of a coherent train of high-frequency vortices of alternating sign in shear layer stabilization, as opposed to a train of vortices of the same sense. Dandois, Garnier & Sagaut (2007) carried out a comprehensive direct numerical simulation and large-eddy simulation study of separation control over a rounded ramp by both high- and low-frequency actuation. They showed that high-frequency actuation induces suppression in production of TKE along with reduction in the energy of the large-scale motions and a concomitant enhancement of the energy of the small-scale motions which was attributed to the altered stability of the base flow, in accord with the hypothesis of Stanek *et al.* (2002).

The present paper focuses on the coupling mechanisms of small-scale high-amplitude actuation on the local and global near-field evolution of a plane turbulent shear layer that forms off a backward-facing step. This work builds on the preliminary investigations of Vukasinovic, Lucas & Glezer (2004, 2005), Rusak & Eisele (2005) and Lucas (2005). The main objective is to gain a better understanding of the evolution of the actuation within the boundary layer upstream of the ensuing shear layer and its effect on the suppression of large-scale vortical motions in its near field. The actuation frequency is at least three times higher than the highest 'natural' frequency of the present shear layer and its Strouhal number $St_{\theta 0} = f_d\theta_0/U_0$ (based on the momentum thickness of the boundary layer at the step edge θ_0 and the free-stream speed U_0) is 0.05. Linear stability analysis of the role of frequency and amplitude in the evolution of excitation disturbances within the shear layer are discussed in § 2. The experimental set-up and flow diagnostics are presented in § 3, and the evolution of the baseline flow (in the absence of actuation) and the effects of small-scale actuation are described in §§ 4 and 5, respectively. Finally, concluding remarks are presented in § 6.

https://doi.org/10.1017/S0022112010001023 Published online by Cambridge University Press

2. Some comments on shear layer stability

As noted in § 1, actuation of small-scale (high-frequency) motions in a free shear flow can lead to a significant reduction in the energy of low-frequency perturbations and perhaps render the base flow stable to these perturbations. Therefore, it is attractive to consider the extension of linear or nonlinear stability analyses that have been used to model the evolution of low-frequency excitation to also model the effects of high-frequency excitation (Stanek *et al.* 2002; Rusak & Eisle 2005). In fact, as shown by Rusak & Eisle (2005), this approach can lead to a single stability analysis that describes the influence of a wide band of excitation frequencies on the evolution of both large and small scales within the shear layer.

The Appendix outlines multi-scale modelling (based on the Navier–Stokes equations in the vorticity and stream function formulation) of the linearized dynamics of perturbations in a two-dimensional shear layer that forms downstream of a backward-facing step. The shear layer flow is characterized by an initial dimensionless natural frequency $\omega_{n,0}$ at the layer origin $x=0$, scaled with far-field speed U_0 and the boundary layer momentum thickness θ_0 at $x=0$. The natural frequency of the shear layer decreases monotonically with distance from $x=0$ due to the increase in the width of the layer. Upstream excitation is characterized by a dimensionless (real) frequency $\omega=2\pi f_d\theta_0/U_0=2\pi St_{\theta 0}$ where f_d is the actuation frequency. A linear parabolic stability equation (LPSE (A 8), in the Appendix) shows that the resulting perturbation stream function is composed of a periodic train of vortices that are advected downstream and described by ψ_1, where the wavelength and perturbation amplitude vary with ω, and a global mode described by ψ_g that is centred near the reattachment point where the separated shear layer transitions to a wall boundary layer. The linear growth of perturbations within the shear layer ends when the excitation frequency is approximately $2\omega_{n,0}$. This frequency is exactly $2\omega_{n,0}$ only for a shear layer having a hyperbolic tangent velocity distribution (Michalke 1964).

At 'low' actuation frequencies, when ω is less than $2\omega_{n,0}$, the solution exhibits three streamwise domains along the shear layer. In the first, 'near-field' domain the excitation frequency at each streamwise position x is less than about twice the local natural frequency at that position and the perturbation amplitude grows with distance from $x=0$. In the second, 'mid-field' domain the actuation frequency at each streamwise position is greater than twice the local natural frequency at that position and the perturbation decays with distance from the step. The third domain is the 'far field', where the perturbations from the mid-field continue to decay, yet supplying energy to the global mode of the base flow, which in turn, provides upstream feedback from the reattachment of base flow.

To demonstrate this evolution, the shear layer of the backward-facing step base flow at $Re_{\theta 0}=9.5$ (corresponding to $Re=1000$ based on the step size $H=105\theta_0$) is considered. In this case it is found that $\omega_{n,0}=0.038$ or $St_{\theta 0}=0.006$ and the natural frequency decreases along the shear layer to $0.5\omega_{n,0}$ at $x/\theta_0=185$ and to $0.25\omega_{n,0}$ at $x/\theta_0=700$. Using (A 9), the response ψ_1 of this shear layer flow is computed for various excitation frequencies ($\omega=0.25\omega_{n,0}, 0.5\omega_{n,0}, 0.75\omega_{n,0}$ and $\omega_{n,0}$). The streamwise variation of the dimensionless cross-stream perturbation kinetic energy $E=\int_{-105\theta_0}^{+\infty}(u'^2+v'^2)\,\mathrm{d}y$ for various excitation frequencies is shown in figure 2(*a*) (here E is rescaled for all ω so that $E=1$ at $x=0$). The slight waviness of E is a result of the periodic vortex train. At low excitation frequencies ($\omega<2\omega_{n,0}=0.076$), the perturbation amplitude and energy increase with streamwise distance from the origin, reach a maximum where the excitation frequency ω is about twice the local

https://doi.org/10.1017/S0022112010001023 Published online by Cambridge University Press

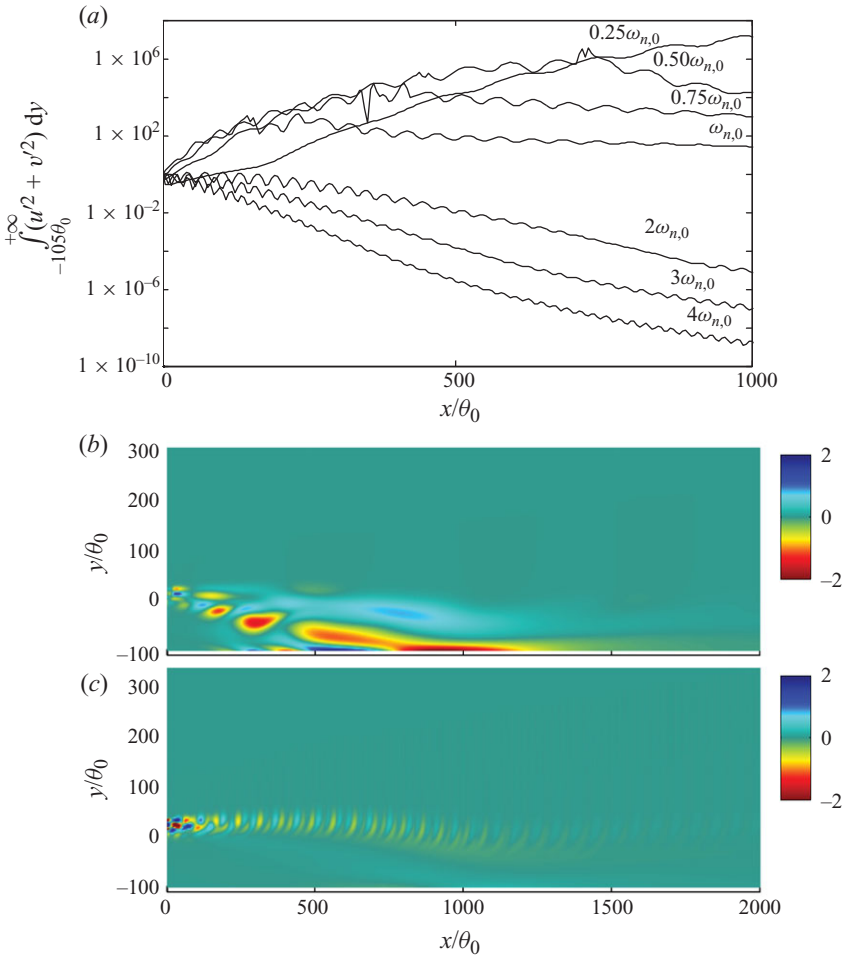


FIGURE 2. (Colour online) Computed response of a backward-facing step flow ($Re_{\theta 0}=9.5$, $\omega_{n,0}=0.038$) to upstream actuation: (*a*) cross-section integrated perturbations kinetic energy computed using LPSE along the shear layer at several excitation frequencies, and numerically simulated vorticity perturbation field at (*b*) $\omega=0.25\omega_{n,0}$ and (*c*) $\omega=2\omega_{n,0}$.

natural frequency and then decay farther downstream while feeding energy to the global mode. Furthermore, the position where the perturbation amplitude has a local maximum shifts upstream as the actuation frequency ω increases towards the threshold level $2\omega_{n,0}=0.076$.

An example of the global evolution of the perturbation vorticity along the shear layer at $Re_{\theta 0}=9.5$ and 'low' excitation frequency $\omega=0.25\omega_{n,0}$ ($St_{\theta 0}=0.0015$) was computed using the direct numerical simulation code of Hawa & Rusak (2001) based on (A 1)–(A 5) and is shown in figure 2(*b*). The inlet condition (A 2) is used as an unsteady excitation which represents a time-periodic train of vortices that form within the upstream boundary layer and enter the shear layer. This vortex train is described by $\kappa=0.05$, $g(y,t)=\{1-(2\pi/0.1)\cos[2\pi(y+0.03)/0.1]\}\sin(\omega t)$ for $0.03\leqslant y\leqslant 0.13$ and $g(y,t)=0$ elsewhere. The perturbation's growth ($0<x/\theta_0<600$), its decay and feed of low-frequency energy to the global mode ($x/\theta_0>600$) and the feedback effect of the global mode are evident in figure 2(*b*).

https://doi.org/10.1017/S0022112010001023 Published online by Cambridge University Press

As noted in § 1, traditional control of free shear flows has relied primarily on the amplification of fundamental instability modes within the receptivity range of the base flow where the excitation frequencies typically range from the most unstable frequency $f_{n,0} = \omega_{n,0}/2\pi$ at the shear layer origin down to a fraction of that value that is amplified farther downstream (Ho & Huerre 1984).

The natural receptivity of the shear layer results in a limiting shortest near-field domain that is related to excitation at the highest possible frequency within the receptivity band (about $2f_{n,0}$) and is typically dominated by coherent motions at the most amplified frequency. The analysis (in the Appendix) shows that when the excitation frequency is higher than about twice any of the natural frequencies along the shear layer (i.e. when $\omega > 2\omega_{n,0}$), the 'natural' near-field behaviour is suppressed. In this case, the perturbation amplitude decays with distance from the shear layer's origin, feeding much less energy to the global mode of the baseline backward-facing step flow than the naturally amplified low-frequency modes. The computed streamwise variation of the dimensionless cross-stream perturbation kinetic energy E for excitation frequencies $\omega > 2\omega_{n,0} = 0.076$ (figure 2*a*) show that the perturbation amplitude and energy decay with distance from the shear layer's origin. The simulated global evolution of the perturbation vorticity along the shear layer at 'high' excitation frequency $\omega = 2\omega_{n,0}$ ($St_{\theta 0} = 0.012$ with $\kappa = 0.05$ at $Re_{\theta 0} = 9.5$) is shown in figure 2(*c*). The perturbations remain relatively strong and decay slightly within the range $0 < x/\theta_0 < 100$, followed by a significant decay within the domain $100 < x/\theta_0 < 500$ and a considerably lower feed of energy to the global mode in the domain $x/\theta_0 > 500$ as predicted by (A 8). These results show that unlike the excitation at 'low' frequencies, 'high-frequency' excitation eliminates much of the feedback from the reattachment of the baseline flow.

It is noted that the increase in the actuation frequency leads to an inherent enhancement of mixing within the shear layer by 'direct' excitation of small-scale motions close to its origin and relies less on 'indirect' mixing by the ultimate breakdown of the large-scale structures. Furthermore, it is also clear that owing to the inherent attenuation of the high frequencies along the layer, the actuation has a relatively small effect on the evolution of the base flow if the actuation amplitude is sufficiently low. Therefore, when the actuation frequency is above the shear layer's receptivity band, it is typically necessary to increase the actuation level in order to alter the stability characteristics of the base flow. Large-amplitude excitation is also necessary to overcome low amplification rates when actuation is applied at frequencies that are substantially below the baseline 'fundamental' frequency (Ho & Huerre 1984). The present work considers three characteristic actuation levels that induce small, moderate and strong changes in the mean velocity field near the layer's origin. It is shown that excitation of high-frequency modes results in a near-field increase in cross-stream width and reductions in the receptivity to low-frequency disturbances and feedback effects of the global mode. High-frequency actuation at finite levels is clearly characterized by nonlinear interactions between the high- and low-frequency modes and the global mode of the flow. The analysis of these nonlinear interactions is the subject of a forthcoming paper.

3. Experimental set-up and flow diagnostics

The present investigation is conducted in a low-speed closed return wind tunnel that is specifically designed for high-resolution particle image velocimetry (PIV) measurements. The tunnel test section measures 25 cm × 41 cm × 132 cm, has a

https://doi.org/10.1017/S0022112010001023 Published online by Cambridge University Press

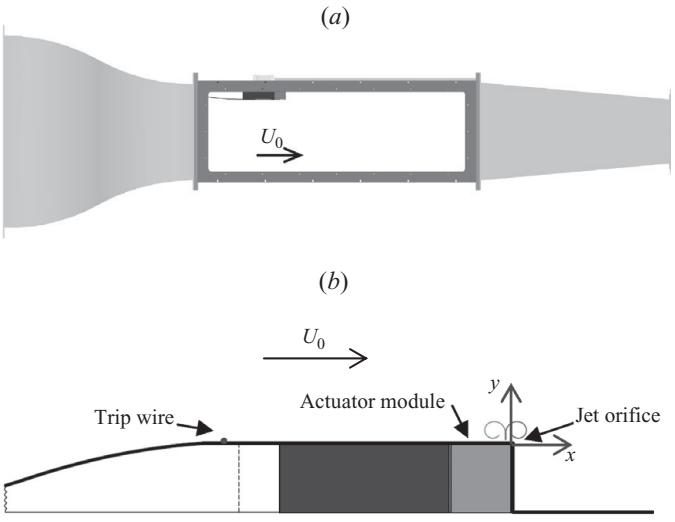


FIGURE 3. Schematic drawings of the test section (*a*) and of the (inverted) flow geometry (*b*).

free-stream speed of up to $35\,\mathrm{m\,s^{-1}}$ and the free-stream turbulence level is lower than 0.5 %. A single-stream shear layer is generated by flow separation off the edge of a backward-facing step on the top wall of the test section, as shown in figure 3(*a*). The step spans the full width of the test section and its height is $H = 50.8\,\mathrm{mm}$ (for convenience, the present results are presented in a flipped view as shown in figure 3*b*). The boundary layer upstream of the step is turbulent as a result of a 1.0 mm diameter trip wire that is mounted at 350 mm upstream from the step edge. In the absence of actuation, the boundary layer thickness at the step edge is $\delta_0 = 4.7\,\mathrm{mm}$, the displacement thickness is $\delta_0^* = 0.49\,\mathrm{mm}$, the momentum thickness is $\theta_0 = 0.35\,\mathrm{mm}$ and the Reynolds number is $Re_{\theta 0} \approx 312$.

Actuation was effected by a spanwise cluster of six individually addressable synthetic jet modules that are integrated into and issue normal to the step surface. Each module is driven by two piezoelectric disks through two adjacent rectangular orifices 1.8 mm apart whose long sides (18.3 mm) are aligned in the spanwise direction, and the (streamwise) width of each orifice is $b_j = 0.38\,\mathrm{mm}$. The orifices form a spanwise-segmented array that spans about 95 % of the test section and is located 8 mm ($21b_j$) upstream of the step edge. Each module is calibrated outside the test section by measuring the streamwise velocity distribution above the exit orifice using a miniature hot-wire sensor. These data are used to compute the characteristic jet velocity U_j which is averaged over the expulsion part of the actuation cycle. Concomitant measurements of the total pressure at the orifice (using a miniature pressure probe) are used for *in situ* assessment of the jet speed between experiments. The operating frequency of the actuators is within the range $St_{\theta 0} = f_d\theta_0/U_0 = 0.012 - 0.06$ (in the present experiments, $f_d = 2\,\mathrm{kHz}$, $St_{\theta 0} = 0.05$). The magnitude of the actuation is assessed from the momentum coefficient R_μ which measures the ratio of the momentum flux per unit width through the jet and the adjacent boundary layer $R_\mu = U_j^2 b_j/[U_0^2(\delta_0 - \delta_0^* - \theta_0)]$. Three levels of R_μ are used, namely $R_\mu = 0.06$ (low), 0.35 (moderate) and 0.63 (high).

In the present work, the actuation is applied to the shear layer by modulation of the vorticity flux through the upstream boundary layer which is merely used as medium for advection of the actuation into the ensuing shear layer. Because of the relatively short residence length, the effects of the boundary layer stability characteristics

https://doi.org/10.1017/S0022112010001023 Published online by Cambridge University Press

(e.g. amplification) are not significant. Although the temporal and spatial characteristics of the vorticity distribution (and hence of the vorticity flux) within the boundary layer are clearly affected by its Reynolds number which may be relatively low (in the present experiments $Re_{\theta 0} \approx 312$), the strength of the actuation is actually measured by the degree of modulation of the (given) flux. It is noteworthy that dissipative, small-scale actuation effected by synthetic jets was successfully implemented in several flow configurations at significantly higher-boundary-layer Reynolds numbers (e.g. Shaw, Smith & Saddoughi 2006; Vukasinovic *et al.* 2009), indicating that the key element of the actuation is the ability to temporally modulate the boundary layer's vorticity flux, regardless of its Reynolds number.

The flow field is mapped using PIV where (as shown in figure 3*a*) the measurement domain in the cross-stream x–y plane is within $-0.5 < y/H < 0.5$ and $-0.5 < x < H < 2.5$ (the CCD camera and the laser-sheet are positioned by computer-controlled traverse mechanisms). The PIV images comprise eleven partially overlapping fields having image resolution of 26.9 μm pixel^{-1}. Finer resolution (9.3 μm pixel^{-1}) is used to investigate the interactions between the actuation vortices and the crossflow boundary layer and to estimate turbulent dissipation. The time-averaged PIV measurements were based on ensembles of 400–500 image pairs, while each phase of the phase-locked PIV measurements was based on an ensemble of 300 image pairs (the uncertainties in the measured time-averaged streamwise and cross-stream velocity components are estimated to be 3 % and 4 %, respectively). Spectral characterization of the flow is accomplished using a single-sensor hot-wire anemometry within the cross-stream plane at eight streamwise stations: $x/H = 0.1$, 0.2, 0.4, 0.6, 0.8, 1, 1.18 and 1.38. Power spectral densities (p.s.d.) were computed from ensemble averages of the spectra of 80–100 time records yielding a frequency resolution of 1.8 Hz (with estimated uncertainty of 4 %).

4. Characterization of the baseline flow

The baseline flow at $Re_{\theta 0} = 312$ ($Re_H = 43\,000$) in the absence of actuation is characterized using PIV within the domain $-0.5 < x/H < 2.5$, $-0.5 < y/H < 0.5$. Figure 4(*a*) shows a raster plot of the time-averaged vorticity field along with cross-stream distributions of velocity vectors. As the boundary layer on the surface of the step evolves into the single-stream shear layer, its cross-stream spreading is asymmetric about $y = 0$ owing to strong entrainment on the low-speed side which biases the cross-stream spreading of the shear layer towards the horizontal surface. The base flow is clearly not self-similar, either in the near field as the flow separates from the step, or in the far field owing to the length scale associated with the step. Figure 4(*b*) shows a raster plot of the corresponding two-dimensional estimate of the TKE in the baseline flow. A narrow domain of high TKE immediately downstream from of the step edge ($x/H < 0.6$) marks the mixing of the boundary layer. Once the remnants of the boundary layer diffuse, there is a drop in the magnitude of the TKE. Farther downstream ($x/H > 1.2$), the TKE increases as the shear layer is formed and small-scale motions begin to evolve. The highest TKE levels are consistently higher within the shear layer core and the highest level appears at the downstream end of the measurement domain and is associated with the initial ('natural') rollup of the shear layer vortices.

The evolution of the baseline flow was computed within the domain $-1 < y/H < 5$ and $-5 < x/H < 20$, using a Fluent code with k-ε model on a uniform mesh with $625 \times 120\,(x, y)$ grid points (the computed results exhibited similar convergence to

https://doi.org/10.1017/S0022112010001023 Published online by Cambridge University Press

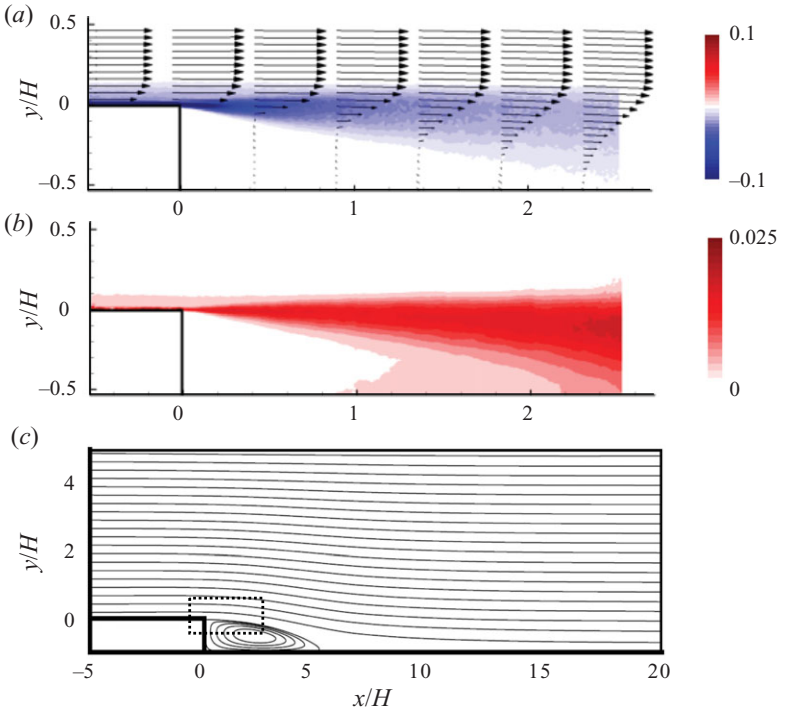


FIGURE 4. (Colour online) (*a*) Raster plots of the measured spanwise vorticity field $\zeta_Z\theta_0/U_0$ with equidistant cross-stream velocity profiles, (*b*) a two-dimensional estimate of the TKE, k/U_0^2, and (*c*) computed streamlines of the baseline flow.

finer meshes) and with an inlet cross-stream velocity distribution $U(x/H=-5, y)$ taken from the experimental measurements. It is found that the computed mean velocity distributions are similar to the measured time-averaged distributions within the domain $-0.5 < y/H < 0.5$ and $0 < x/H < 2.5$ and contours of the computed stream function are shown in figure 4(*c*). These data indicate that the separated flow downstream of the step reattaches at $x/H \sim 5.5$, which is in accord with experimental wall pressure measurements (not shown).

Two global parameters that characterize the spreading of the shear layer are shown in figure 5, namely the streamwise growth of the layer's local width $w(x)$ and momentum thickness $\theta(x)$. The shear layer width is defined as the difference between cross-stream elevations where the local (mean) velocity is 0.95 and $0.05U_0$. These data show that the streamwise growth rate of the layer can be characterized by $\mathrm{d}w/\mathrm{dx} \sim 0.179$ and $\mathrm{d}\theta/\mathrm{dx} \sim 0.032$, which are comparable to other measurements in single-stream (e.g. Morris & Foss 2003) and two-stream (e.g. Roberts & Roshko 1985) shear layers indicating that the near-field evolution of both flows are similar. The width of the computed base flow (not shown) is in good agreement (within 5 %) with the measured data over the entire measurement domain.

The natural receptivity of the baseline shear layer to external disturbances is assessed from spectral analysis of hot-wire measurements in the baseline flow (in the absence of actuation). Cross-stream distributions of velocity power spectra that are measured at eight streamwise stations through $x/H = 1.38$ are used to form raster plots of the energy content in the cross-stream (x–y) plane for each of the spectral components at 50, 100, 200 and 300 Hz (figure 6*a–d*, respectively). These distributions clearly

https://doi.org/10.1017/S0022112010001023 Published online by Cambridge University Press

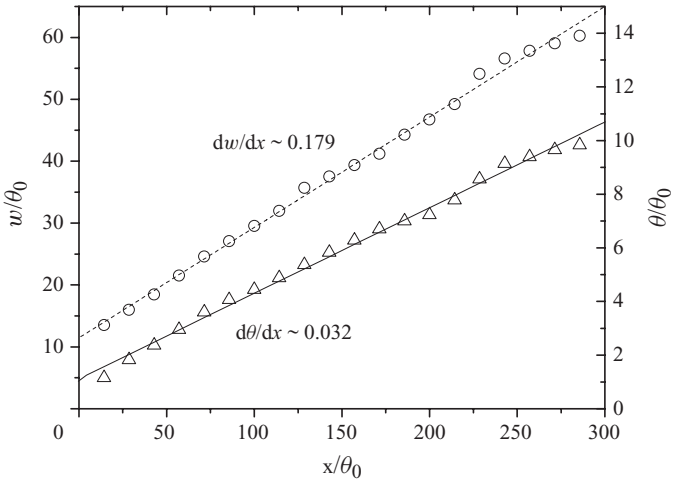


FIGURE 5. Streamwise variation of the measured baseline shear layer width w (○) and momentum thickness θ(Δ).

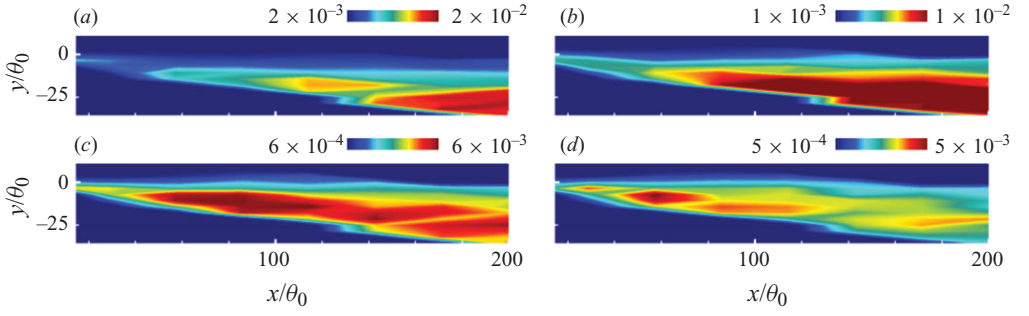


FIGURE 6. (Colour online) Raster plot of the spectral energy measured in the base flow at $f = 50$ Hz (*a*), 100 Hz (*b*), 200 Hz (*c*) and 300 Hz (*d*).

show that the most amplified component (within the measurement domain) is 200 Hz (figure 6*c*). As predicted by stability analysis (cf. in § 2), the lower frequencies 100 Hz (figure 6*b*) and 50 Hz (figure 6*a*) become amplified (and reach their peak magnitudes) farther downstream (at $x/\theta_0 > 100$ and 140, respectively). Also, it is noteworthy that the higher spectral component at 300 Hz becomes most amplified relatively close to the step edge ($x/\theta_0 \approx 60$), indicating that the higher spectral components saturate and begin to decay near the shear layer's origin as depicted in figure 2(*a*).

Each spectral raster plot in figure 6 yields estimates of the streamwise domain of amplification and the corresponding upstream and downstream amplification boundaries within the measurement domain as shown in figure 7. The streamwise locations at which spectral components f_n are most amplified based on the stability analysis of the time-averaged flow field (cf. § 2) are also shown in figure 7. As expected, these data show that the (most amplified) 'natural' frequency decreases with distance from the step, corresponding to the cross-stream spreading of the shear layer (cf. figure 5). The analysis predicts that the most amplified frequency decreases with increasing shear layer momentum thickness θ as $f_n \sim 0.016 \times U_0/\theta$. While the overall agreement between the measured amplification boundaries and computed amplified

https://doi.org/10.1017/S0022112010001023 Published online by Cambridge University Press

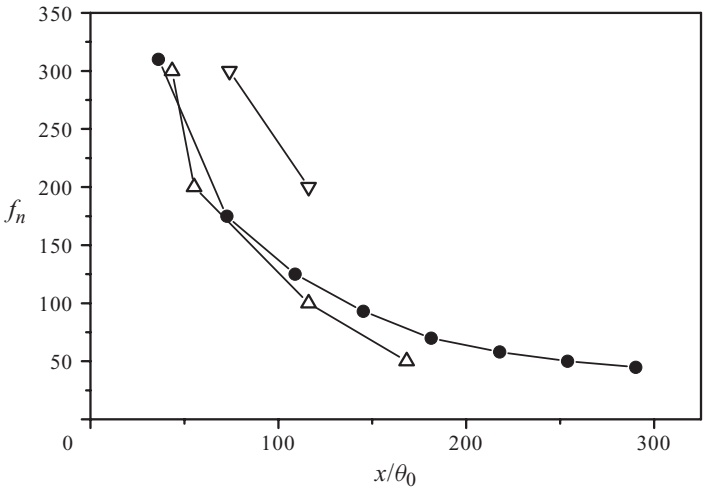


FIGURE 7. The upstream (Δ) and downstream (∇) endpoints of the amplified domains of (measured) spectral components at $f = 50$, 100, 200 and 300 Hz (cf. figure 6), and the corresponding most amplified frequencies based on a local stability analysis (●).

spectral peaks is good, the results of the linear stability analysis are better aligned with the upstream boundary of the experimental data.

5. Direct small-scale actuation

5.1. *The interaction of the actuation jet with the plane shear layer*

Direct actuation of small-scale motions in the separating shear layer is effected by rapid time periodic ejection of trains of small-scale counter-rotating vortex pairs that are generated by the spanwise array of synthetic jet actuators described in § 2. The interaction of these vortices with the crossflow is investigated using high-resolution PIV measurements within a field of view measuring approximately $25b_j$ on the side, yielding velocity vectors on a square grid with $0.4b_j$ spacing. The measurements are taken phase-locked to the actuation waveform in phase increments of $\Delta\phi = 20°$.

Raster maps of the phase-averaged spanwise vorticity concentrations of the ejected vortices in the absence and presence of a crossflow are shown in image sequences in figure 8(*a–e*) and figure 8(*f–j*), respectively. Similar to the observations of Smith & Glezer (1998), in the absence of a crossflow the counter-rotating vortex pair that forms during each actuation cycle is advected away from the orifice under its own self-induced velocity as shown in figure 8(*a–e*). The interaction of the vortex pair with the crossflow boundary layer upstream of the step edge is evident in figure 8(*f*) ($\phi = 80°$, about $0.22T_{jet}$ after the start of the expulsion cycle, $\phi = 0°$). Compared to figure 8(*a*), the symmetry of the vortex pair is disrupted as the clockwise (CW) vortex is strengthened while the counter-clockwise (CCW) vortex is weakened by the predominant CW vorticity in the boundary layer (note that the CW vortex from the previous cycle is still visible at the downstream end of the measurement domain). As the actuation cycle progresses (figure 8*g*, $\phi = 140°$), the larger CW vortex begins to be advected in the streamwise direction at an elevation of $y/\delta_0 = 0.25$ while the weaker CCW vortex begins to translate over and ultimately stretches around the CW vortex core as is evidenced in the next phase in figure 8(*h*) ($\phi = 180°$). Here, part of the elongated CCW vortex is located above the core and its leading edge is almost aligned with the CW vortex. It is notable that the CW vortex appears to remain at a nearly

https://doi.org/10.1017/S0022112010001023 Published online by Cambridge University Press

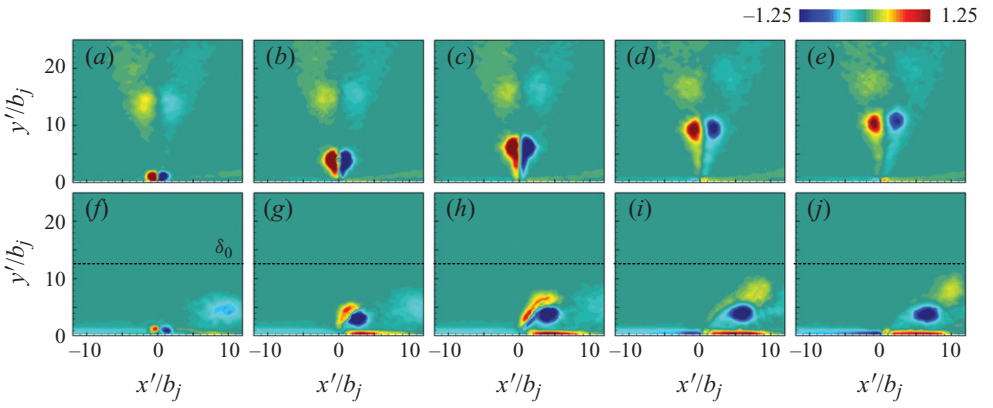


FIGURE 8. (Colour online) Raster plots of the phase-averaged vorticity $\zeta_z(\phi)\theta_0/U_0$ of an actuation jet formed at $f_d = 2000$ Hz in the absence (*a–e*) and presence (*f–j*) of crossflow at $\phi = 80°$ (*a*, *f*), 140° (*b*, *g*), 180° (*c*, *h*), 260° (*d*, *i*) and 300° (*e*, *j*). The jet orifice ($b_j = 381\,\mu$m) is located at $x' = y' = 0$. The boundary layer thickness of the baseline flow δ_0 is denoted by a dashed line.

constant elevation above the surface ($y/\delta_0 = 0.3$), and its estimated advection speed is about $0.5U_0$. It is also noteworthy that the passage of the CW vortex over the surface is accompanied by a region of reversed flow beneath it as indicated by a thin wall layer of CCW vorticity. In the meantime, the CCW vortex which is at a higher elevation is advected at a higher speed (and therefore farther downstream) and by $\phi = 260°$ (figure 8*i*), the remnants of the CCW vorticity are rolled into a core that has about the same diameter as the CW vortex, but with a much weaker vorticity distribution.

Given the significant difference in the relative strength of the CW and CCW vortices, it appears that the actuation of the separating shear layer downstream of the step is effected by the train of CW vortices. These vortices interact with and modulate a vorticity layer having predominantly the same sense. As discussed below, for a given boundary layer thickness, the magnitude of the modulation depends on the strength of the CW vortex train and therefore on the jet/boundary layer momentum flux ratio R_μ. For the images shown in figure 8(*f–j*), R_μ is selected to be 0.08 so that the characteristic diameter of the actuation vortices is smaller than the boundary layer thickness and the vortices are advected within the boundary layer. This momentum flux ratio is just slightly above the lowest level of the three characteristic actuation levels in the present investigation ($R_\mu = 0.06$, 0.35 and 0.63).

The dynamics of the interactions between the vortex train and the shear layer is assessed from PIV measurements that are taken phase-locked to the actuation waveform within the streamwise domain $-30 < x/\theta_0 < 115$ at the three jet momentum flux ratios. Maps of the resulting spanwise vorticity concentrations are shown in figure 9(*a–c*) for $R_\mu = 0.06$, 0.35 and 0.63, respectively. At the low-momentum flux ratio (figure 9*a*), the interaction of the actuator vortices with the crossflow is primarily confined to the wall boundary layer (cf. figure 8). The CW vorticity layer near the downstream edge of the step is temporally and spatially modulated with successive CW vortices which have a nominal diameter $d_v/\delta_0 \approx 1/3$ and are separated by the weak remnant of the CCW vortices. The coherence of the CW vortices diminishes rapidly within the shear layer, and by $x/\theta_0 \approx 20$ the vorticity within the shear layer appears to be featureless. As R_μ is increased to 0.35 (figure 9*c*), the CW actuation

https://doi.org/10.1017/S0022112010001023 Published online by Cambridge University Press

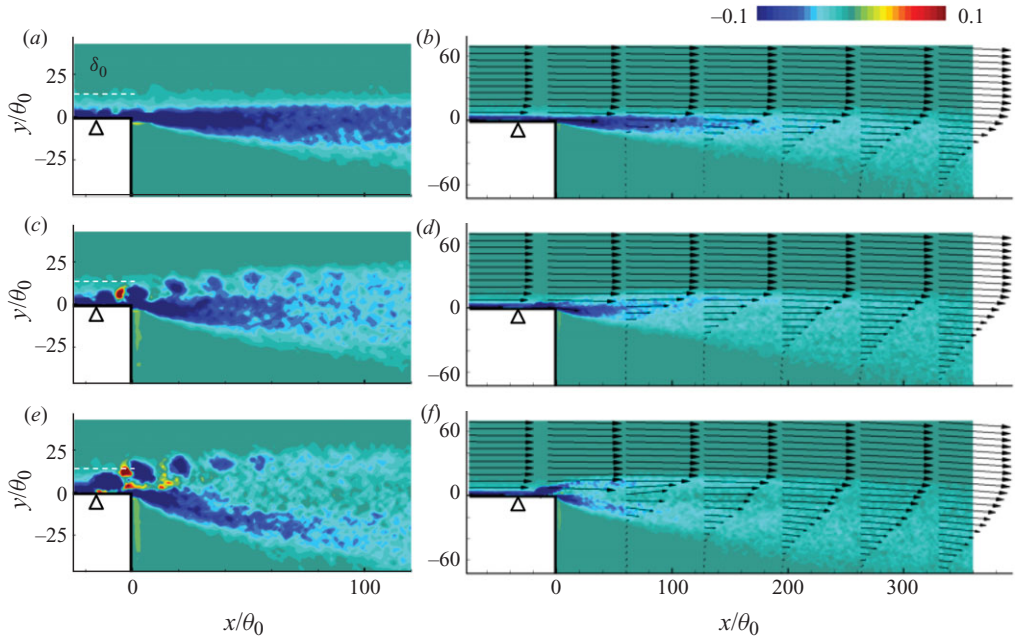


FIGURE 9. (Colour online) Phase-averaged (*a*, *c*, *e*) and ensemble-averaged (*b*, *d*, *f*) vorticity fields $\zeta_Z\theta_0/U_0$ with overlaid velocity profiles for the actuated flow at $St = 0.05$ and $R_\mu = 0.06$ (*a*, *b*), 0.35 (*c*, *d*) and 0.63 (*e*, *f*). The actuator orifice is marked by a triangle, and the boundary layer thickness of the base flow δ_0 is denoted by a dashed line.

vortices have larger vorticity concentrations and diameter ($d_v/\delta_0 \approx 1/2$). While the vortex train remains within the boundary layer up to the downstream edge of the step, the CW vortices begin to protrude through the edge of the boundary layer as the shear layer is formed. These vortices are advected faster than the corresponding actuation vortices in figure 9(*a*) because they interact with the separating shear layer along its high-speed edge. It is remarkable that the vortex train maintains its coherence along the edge of the shear layer through most of the measurement domain in figure 9(*c*), followed by 'merging' at the high-speed edge at $x/\theta_0 > 100$.

Further increase in the jet momentum flux ratio ($R_\mu = 0.63$) (figure 9*e*) leads to protrusion of the jet vortices through the boundary layer just upstream of the step edge, and they are advected above the high-speed edge of the forming shear layer until they begin to lose their coherence (at least relative to the actuation frequency) by $x/\theta_0 \approx 75$. As a result of this interaction, the shear layer spreads farther towards the low-speed side (e.g. compare figures 9*a* and 9*e*) which is accompanied by a reduction in the magnitude of the vorticity concentrations in the upper half of the shear layer and by increased entrainment from the low-speed side as manifested by the upward flow along the vertical wall of the step.

The phase-averaged data are accompanied by maps of the time-averaged spanwise vorticity concentrations (along with overlaid cross-stream velocity distributions) in the domain $-75 < x/\theta_0 < 360$ as shown in figures 9(*b*), 9(*d*) and 9(*f*). At the low momentum flux ratio ($R_\mu = 0.06$) (figure 9*b*), there is little or no difference between the time-averaged velocity and vorticity fields of the unforced and forced flows (the vorticity magnitude decreases only slightly in the forced flow). However, as the momentum flux ratio is increased ($R_\mu = 0.35$) (figure 9*d*), and the actuation vortices interact with the high-speed edge of the forming shear layer, the shear layer spreads more towards the

https://doi.org/10.1017/S0022112010001023 Published online by Cambridge University Press

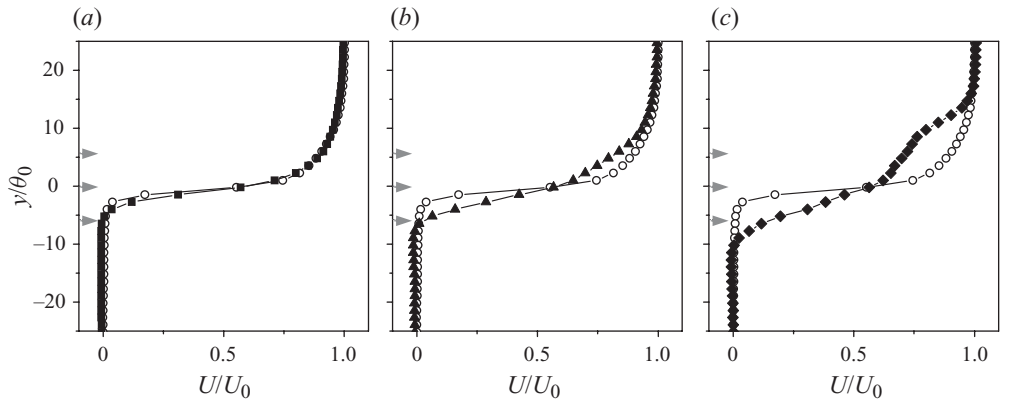


FIGURE 10. Time-averaged streamwise velocity distributions at $x/\theta_0 = 14.8$ in the absence (○) and presence of actuation at $St = 0.05$ and $R_\mu = 0.06$ (■), 0.35 (▲) and 0.63 (◆). The arrowheads mark the cross-stream elevation of the spectra in figure 14.

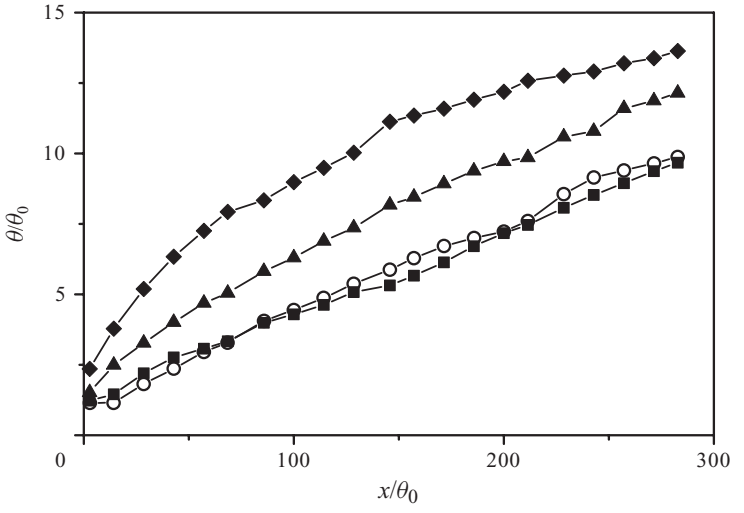


FIGURE 11. Streamwise variation of the shear layer momentum thickness for the baseline (○) and the actuated flows at $St = 0.05$ and $R_\mu = 0.06$ (■), 0.35 (▲) and 0.63 (◆).

low-speed side and the magnitude of the vorticity within the shear layer decreases. At the highest R_μ considered here, the vorticity layer associated with the actuation is separated from the shear layer (figure 9*f*), but they merge at $x/\theta_0 > 200$. These data indicate that the streamwise location of the interaction between the actuation jet and the ensuing shear layer downstream of the step can be adjusted by the jet momentum.

5.2. *Modification of the mean flow field*

One of the important consequences of small-scale actuation from the standpoint of inviscid stability analysis and the evolution of vortical structures within the shear layer are the induced changes in the mean flow, which in turn affect (and, as shown below, reduce) the receptivity of the altered flow to broadband disturbances. The effects of the actuation on the mean flow are demonstrated by considering the alteration of velocity distributions and of the characteristic cross-stream scale (figures 10 and 11). Cross-stream distributions of the streamwise velocity that are measured a short

https://doi.org/10.1017/S0022112010001023 Published online by Cambridge University Press

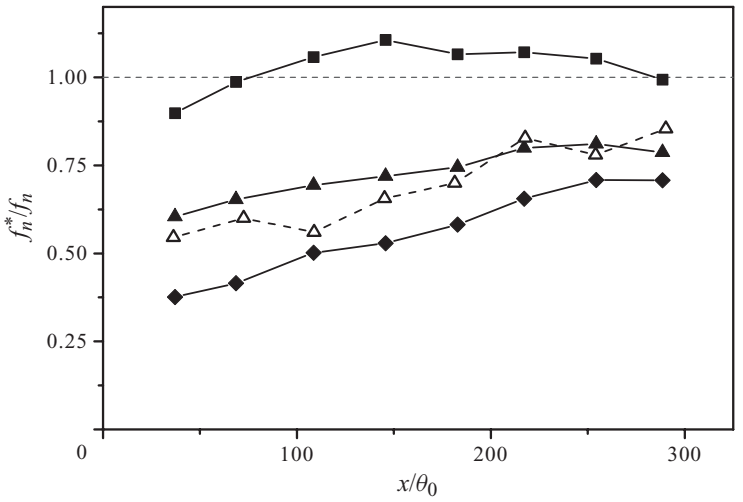


FIGURE 12. Development of the most amplified frequency f_n^* in the forced flow relative to the corresponding frequency f_n in the absence of actuation from measurements at $St = 0.05$ and $R_\mu = 0.06$ (■), 0.35 (▲) and 0.63 (◆), and from linear stability analysis of the measured time-averaged flow at $R_\mu = 0.35$ (△).

distance downstream from the step edge (at $x/\theta_0 = 14.8$) are shown in figure 10. It is remarkable that despite the significant modulation of the vorticity in the boundary layer (cf. figure 9*a*), the low actuation level ($R_\mu = 0.06$) results only in subtle alteration of the mean flow (near $y/\theta_0 = -3$). At moderate actuation level ($R_\mu = 0.35$), the mean velocity distribution begins to exhibit significant changes relative to the base flow which are manifested as cross-stream spreading near the high- and low-speed edges. The distortion is intensified at the high actuation level ($R_\mu = 0.63$), and the presence of the CW actuation vortices near the high-speed edge (cf. figure 9*e*) results in an inflection point near $y/\theta_0 = 10$.

The changes in the characteristic cross-stream scale of the shear layer in the presence of actuation are illustrated by the streamwise variation of the momentum thickness $\theta(x)$ (figure 11). As noted in connection with figure 10, at the lowest actuation level ($R_\mu = 0.06$) there is no significant change in $\theta(x)$ relative to the baseline aside from a small increase that is followed by a similarly small decrease in the domain $x/\theta_0 > 100$. Along with the distributions of the time-averaged velocity and vorticity fields in figure 9(*b*), this indicates that the low actuation level does not alter the mean baseline flow significantly even though it clearly affects some of its dynamic characteristics (e.g. the TKE) (cf. figure 18). As shown in figures 9(*d*) and 9(*f*) and figures 10(*b*) and 10(*c*), higher actuation levels lead to a notable increase in shear layer spreading and consequently in the corresponding momentum thickness. Note that at $R_\mu = 0.35$ $\mathrm{d}\theta/\mathrm{d}x$ is initially higher than in the baseline flow, but it decreases to the baseline level at $x/\theta_0 \approx 100$. The increase in $\mathrm{d}\theta/\mathrm{d}x$ is even more accentuated at $R_\mu = 0.63$ and there is a peak at $x/\theta_0 \approx 140$ which is followed by a somewhat lower growth rate than in the baseline flow.

To illustrate the changes in the stability of the flow that are effected by actuation at moderate and high R_μ, streamwise distributions of the 'most unstable' frequency f_n^* normalized by the corresponding unstable frequency of the baseline shear layer are computed based on the 'global' Strouhal number $St_{\theta g} = 0.016$ of the base flow (figure 12), assuming that $St_{\theta g}$ does not change significantly in the presence of

https://doi.org/10.1017/S0022112010001023 Published online by Cambridge University Press

actuation. At the lowest actuation level there is a small reduction in f_n^* for $x/\theta_0 < 100$ (up to 15 % downstream of the step edge). However, at $R_\mu = 0.35$ and 0.63, f_n^* is significantly lower relative to the base flow (in the absence of actuation). The reduction is strongest immediately downstream of the step followed by a monotonic, almost linear streamwise increase and ultimately asymptotic saturation (to 0.8 and 0.7 for $R_\mu = 0.35$ and 0.63, respectively).

The significant diminution in the magnitude of the most unstable frequency signals a shift in the stability band in the presence of actuation and indicates that the flow becomes more stable to frequencies as low as $0.4 f_n$. This means that small-scale actuation leads to attenuation of a frequency band around the 'natural' frequency of the base flow, rendering the forced flow stable to perturbations within this frequency band. The data for $R_\mu = 0.35$ in figure 12 are compared with the frequencies of the most amplified perturbations that are computed using linear stability analysis of the measured time-averaged velocity field. The close match between the most unstable frequencies predicted by the linear stability analysis and the experimental data is another indication that the flow becomes more stable in the near field and that the unstable frequency band is lowered. Furthermore, the amplification of lower frequencies farther downstream is associated with the formation of vortical structures having larger characteristic scale than in the base flow. It is interesting to note that Dandois *et al.* (2007), who simulated high-frequency control of the flow over a rounded ramp, reported that the actuation resulted in an increase in the 'natural' frequency of the base flow. Even though their stability analysis predicted a reduction in the most amplified frequencies in the presence of actuation, the dominant frequencies in the base flow were actually significantly lower than the stability predictions, perhaps as a result of feedback from the separated flow.

5.3. *Spectral analysis*

As discussed in § 1, small-scale actuation has a profound effect on the spectral content of the base flow by altering the natural receptivity of the shear layer to external disturbances and thereby attenuating low-frequency spectral components. The spectral receptivity in the near field of the present base flow was discussed in connection with figure 6 for spectral components above and below the 'most amplified' frequency. The changes in the receptivity of the flow in the presence of actuation (at $St_\theta = 0.05$) are shown in raster plots of the same spectral components ($f = 50$, 100, 200 and 300 Hz) at $R_\mu = 0.06$, 0.35 and 0.63 (figure 13). Perhaps the most prominent feature of the raster plots of each spectral component is the reduction in magnitude with increasing actuation amplitude. Although this reduction is apparent throughout the entire cross-stream plane, it is most acute near the high-speed edge, and is somewhat milder at the low-speed edge. The stronger effect near the high-speed edge at high momentum ratios is the proximity of the actuation vortex train (cf. figure 9). These effects are particularly apparent at low frequencies ($f = 50$ and 100 Hz) where actuation at $R_\mu = 0.35$ and 0.63 leads to precipitous diminution in spectral magnitudes indicating a significant delay in streamwise amplification. The reduction in the amplitude of the spectral components that are within the 'most amplified' band ($f = 200$ Hz) and above it ($f = 300$ Hz) indicates that the near field (and hence the entire flow) becomes stable to perturbations that would be normally amplified in the near field of the base flow.

An important feature of small-scale actuation is the accelerated transfer of energy from the large to small scales within the flow. It is useful to consider the crossover frequency f_c that separates between spectral bands in which the magnitude of the

https://doi.org/10.1017/S0022112010001023 Published online by Cambridge University Press

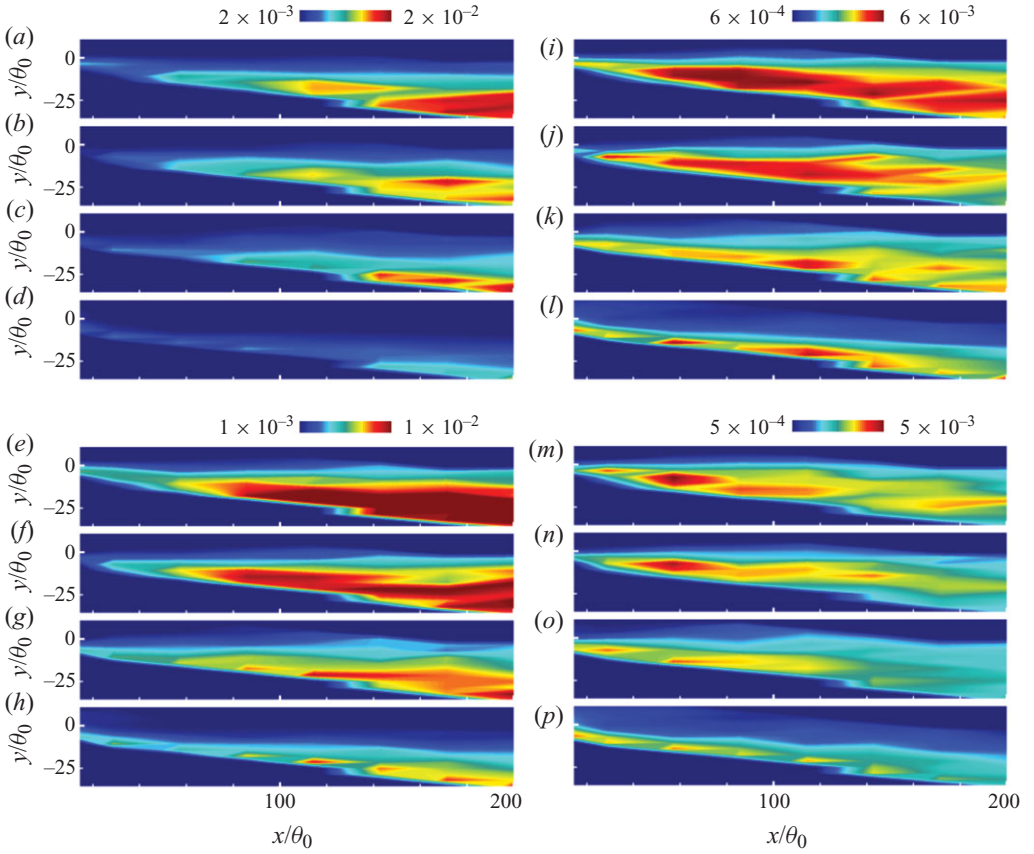


FIGURE 13. (Colour online) Raster plot of spectral energy at $f = 50$ Hz (*a–d*), 100 Hz (*e–h*), 200 Hz (*i–l*) and 300 Hz (*m–p*) in the presence of actuation at $St = 0.05$ and $R_\mu = 0$ (*a*, *e*, *i*, *m*), 0.06 (*b*, *f*, *j*, *n*), 0.35 (*c*, *g*, *k*, *o*) and 0.63 (*d*, *h*, *l*, *p*).

spectral components in the presence of actuation is smaller or larger than in the base flow (cf. figure 1). Figure 14 shows an example of power spectra that are measured in the absence and presence of actuation (at the three actuation levels) near the high- and low-speed edges ($y/\theta_0 = 5.7$ and -5.7) of the shear layer, and at the elevation of the step ($y/\theta_0 = 0$). The absence of discrete low-frequency spectral peaks in the base flow is the result of the proximity of the measurement station to the edge of the step and of deliberate tripping of the upstream boundary layer. The power spectra of the base flow along the low-speed edge and $y = 0$ exhibit significant energy content at low frequencies ($f/f_d < 0.2$, where f_d is the actuation frequency) which is associated with entrainment of low-speed fluid, and the spectral content drops sharply above this band. The magnitude of the spectral components within the same band near the high-speed edge is at least an order of magnitude lower but the spectral components at the high frequencies $f/f_d > 0.5$ are significantly stronger, indicating the presence of small-scale motions near the high-speed edge.

While specific details of the differences between power spectra in the absence and presence of actuation in figure 14 clearly depend on cross-stream elevation, all the spectra of the forced flow exhibit sharp peaks at actuation frequency $f/f_d = 1$ and, concomitantly, a significant increase in the energy content of the small scales even

https://doi.org/10.1017/S0022112010001023 Published online by Cambridge University Press

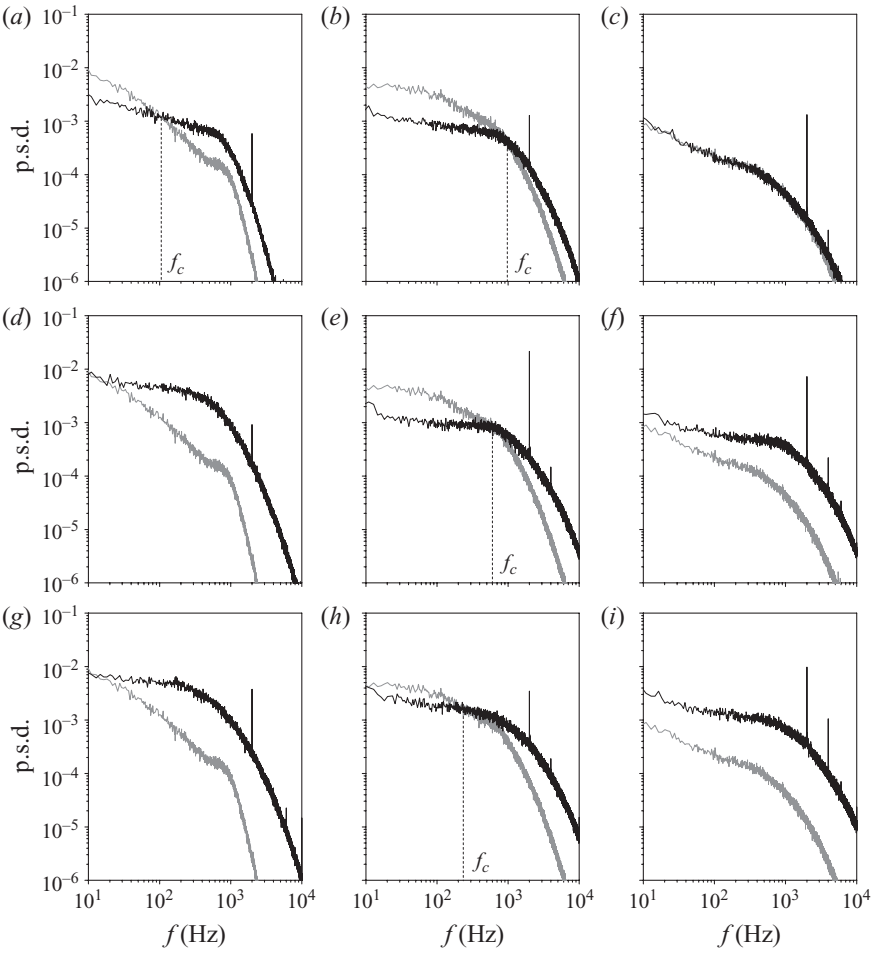


FIGURE 14. Power spectra of velocity fluctuations for the absence (grey) and presence of actuation (black) at $St = 0.05$ and $R_\mu = 0.06$ (*a–c*), 0.35 (*d–f*) and 0.63 (*g–i*), measured at $x/\theta_0 = 14.8$ and $y/\theta_0 = -5.7$ (*a*, *d*, *g*), 0 (*b*, *e*, *h*) and 5.7 (*c*, *f*, *i*) (cf. figure 10).

though the actuation is applied at a discrete frequency. As expected, based on the images in figure 9, the peaks at the actuation frequency are strongest along the high-speed edge of the shear layer and at its centre owing to the formation and passage of the vortex train that is induced by the actuation within the upstream boundary layer. The interaction with these small-scale high-frequency vortices along the high-speed edge of the shear layer leads to influx of small-scale motions and, as shown below, to increased turbulent energy production (figure 18*b*). On the other hand, the increased energy content at the large scales along the low-speed edge is apparently the result of increased shear layer spreading and engulfing of nearly stagnant fluid from below. The small-scale energy content increases further as turbulent energy production increases and the overall energy transfer to the small scales is accelerated.

Perhaps the most intriguing energy redistribution in the presence of actuation takes place within the cross-stream centre of the shear layer (around $y/\theta_0 = 0$), as shown in figures 14(*b*), 14(*e*) and 14(*h*). There is a notable increase in energy content over a broadband of small scales above the crossover frequency f_c that is accompanied

https://doi.org/10.1017/S0022112010001023 Published online by Cambridge University Press

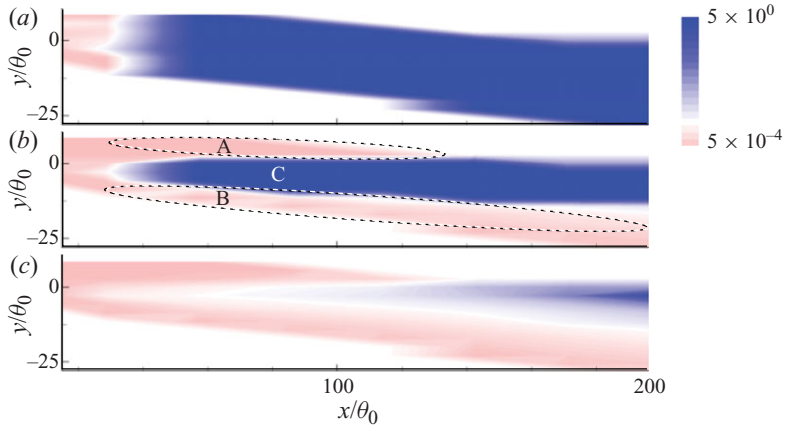


FIGURE 15. (Colour online) Raster plots of the crossover frequency f_c/f_d for actuation at $St = 0.05$ and $R_\mu = 0.06$ (a), 0.35 (b) and 0.63 (c).

by a decrease in the energy of the large scales (low frequencies) below f_c. In fact, as shown in connection with figure 18(a), although the actuation leads to an overall local increase in the (total) TKE, the energy content of the large scales at $y/\theta_0 = 0$ actually decreases while the energy of the small scales increases. Therefore, it can be argued that the actuation affects the energy balance between the low and high ends of the spectrum by accelerating transfer to the small scales and ultimately enhancing dissipation.

Figure 15 shows raster plots of the normalized crossover frequency f_c/f_d such that the bands $f_c < f_d$ and $f_c > f_d$ are marked by red and blue shades, respectively (the low and high limits in which all spectral components of the forced flow are below or above the corresponding components in the base flow are marked by the darkest blue and red, respectively). In addition, the contour $f_c/f_d = 1$ is shown in white to separate the bands in which spectral components below the actuation frequency f_d are attenuated and where spectral components above f_d are amplified. Even when the changes in the time-averaged forced flow are almost indiscernible ($R_\mu = 0.06$, figure 15a), the initial attenuation in the energy of the large scales spreads almost uniformly across the shear layer, and the range of affected scales rapidly spreads to include the small scales. As shown in figure 15(a), the wideband increase in the energy of the small scales immediately downstream from the edge of the step is rapidly dissipated downstream, and the energy over all scales is lowered for $x/\theta_0 > 35$. This broadband suppression of flow fluctuations indicates a stabilizing effect of the actuation. It should be noted, however, that the reduction in spectral energy diminishes as the forced flow relaxes to the unforced (base) state farther downstream (cf. figures 11 and 12).

Figure 15(b–c) indicate that when R_μ is increased, the transfer of energy among the scales is altered. At $R_\mu = 0.35$ (figure 15b) there is a sharp broadening of the range of scales with lower energy in the centre of the shear layer for $x/\theta_0 > 30$, but both the high- and low-speed edges exhibit an overall increase in spectral energy across a wide range of scales. Near the high-speed edge, the domain of increased energy (marked as domain A) is induced by the influx of the high-frequency vortices and increased turbulent energy production (see figure 18b). This domain becomes narrower farther downstream as the high-frequency vortices lose their coherence and dissipate, and turbulent production weakens. Along the low-speed edge (marked as domain B), the

https://doi.org/10.1017/S0022112010001023 Published online by Cambridge University Press

actuation leads to an increase in the spectral energy due to the enhanced spreading of the shear layer, and initially also due to the increased turbulent energy production. Since the energy in this domain is mostly concentrated in the large-scale motions associated with the entrained fluid, the effect of the actuation is not felt within the present measurement domain and little reduction in energy is detected. The strongest decrease in energy occurs within the centre of the shear layer (domain C), which widens slowly in the streamwise direction. As R_μ is increased to 0.63 (figure 15*c*), the three domains in figure 15(*b*) are pushed farther downstream predominantly because the actuation vortex train that is advected along the high-speed edge of the shear layer begins to interact with the layer farther downstream. As a result of the advection of the actuation vortices and the downward deflection of the shear layer, regions of higher amplitude spectral components extend along the high- and low-speed edges of the layer and the reduction of spectral energy in the centre of the shear layer is delayed. Therefore, suppression within domain C is evident only at the downstream end of the measurement domain.

5.4. *Turbulent kinetic energy*

The effects of the actuation on cross-stream distributions of TKE (TKE estimated as $k = (\overline{u'^2} + \overline{v'^2})/2$) are shown in figure 16(*a–c*). Close to the step edge ($x/\theta_0 = 14.5$) (figure 16*a*), the TKE distribution in the base flow has a narrow peak near the centre of the shear layer. Actuation at $R_\mu = 0.06$ results in a slight alteration of the TKE showing a small increase in spreading to the low-speed side and a 16 % reduction in the peak TKE (0.024–0.02) compared to the base flow. As R_μ is increased to 0.35, the shear layer spreading on the low-speed edge becomes more prominent, with the peak TKE exceeding the base level. There is also a significant increase in the TKE level at the high-speed edge due to presence of the CW jet vortices (cf. figure 9*c*).

The cross-stream separation between the induced vortex train and the shear layer is more pronounced at $R_\mu = 0.63$ and is marked by the presence of two distinct cross-stream TKE peaks. A similar double peak is also apparent in the corresponding vorticity concentrations (figure 9*f*). The presence of the small-scale vortex train along the high-speed edge of the shear layer results in a significant increase in TKE within the shear layer (almost twice the base level), and in a stronger spreading towards the low-speed side. It is remarkable that at the next streamwise measurement station ($x/\theta_0 = 29$) (figure 16*b*), the TKE peaks for $R_\mu = 0.63$ are merged, and the overall levels are considerably lower and commensurate with the TKE levels at the lower actuation levels. It is also noteworthy that the TKE peaks at all actuation levels are lower than the peak of the base flow. These trends continue at the last streamwise station ($x/\theta_0 = 72.5$, figure 16*c*), where the direct contribution of the induced vortex train along the high-speed edge weakens, while the shear layer spreading at the low-speed edge increases with R_μ. Of particular note is the diminution in TKE at the low actuation level compared to the unforced flow even though the induced changes in the mean flow due to the actuation are very subtle. As noted in § 1, Dandois *et al.* (2007) reported similar suppression of TKE during high-frequency actuation of the flow over a rounded ramp. These authors observed that following a sharp increase immediately downstream of the actuation source there was a drop in TKE to levels that were below the levels of the base flow. The strong suppression of TKE in the actuated flow gradually diminished downstream and ultimately reached the levels of the base flow.

The earlier work of Vukasinovic *et al.* (2004) established a direct relationship between the strength of the actuation jet and the turbulent dissipation rate ε in the near field. The effect of small-scale actuation on ε is quantified using highly resolved

https://doi.org/10.1017/S0022112010001023 Published online by Cambridge University Press

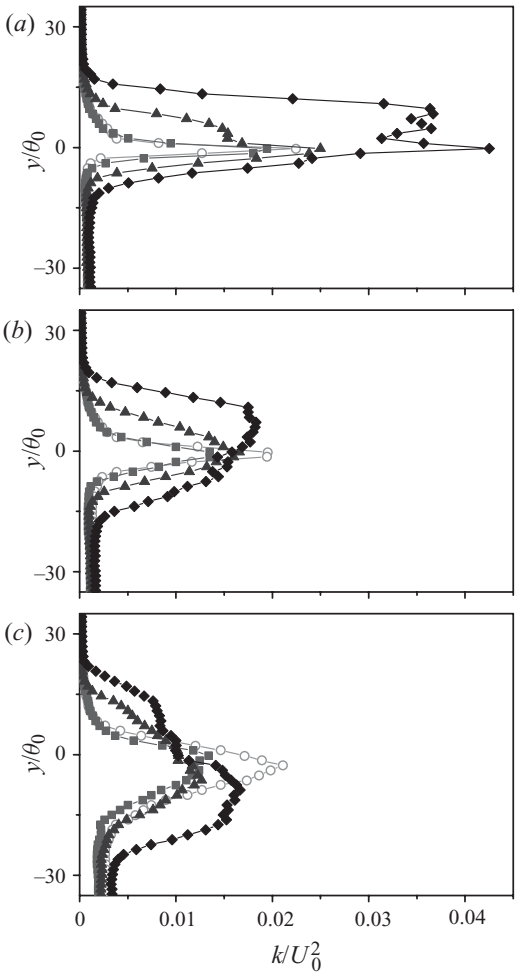


FIGURE 16. Cross-stream distributions of the TKE k/U_0^2 at $x/\theta_0 = 14.5$ (*a*), 29 (*b*), and 72.5 (*c*), in the absence (○) and presence of actuation at $St = 0.05$ and $R_\mu = 0.06$ (■), 0.35 (▲) and 0.63 (◆).

PIV measurements within the formation region of the shear layer in the absence and presence ($R_\mu = 0.63$) of actuation. In the present measurements, the spatial resolution is 150 μm (corresponding to a spectral components at about 46 kHz), which is well within the dissipation range of the flow (cf. figure 14). The 25 mm × 25 mm measurement domain is centred about the step edge and consists of nine partially overlapping views. Assuming that the average magnitudes of the spanwise gradients of velocity fluctuations are similar to the in-plane fluctuations, the turbulent dissipation rate is estimated from the PIV measurements by

$$\varepsilon = 3\nu\left[\overline{\left(\frac{\partial u}{\partial y}\right)^2} + \overline{\left(\frac{\partial v}{\partial x}\right)^2} + 2\overline{\left(\frac{\partial u}{\partial y}\frac{\partial v}{\partial x}\right)}\right] + 4\nu\left[\overline{\left(\frac{\partial u}{\partial x}\right)^2} + \overline{\left(\frac{\partial v}{\partial y}\right)^2} + \overline{\left(\frac{\partial u}{\partial x}\frac{\partial v}{\partial y}\right)}\right]. \tag{5.1}$$

https://doi.org/10.1017/S0022112010001023 Published online by Cambridge University Press

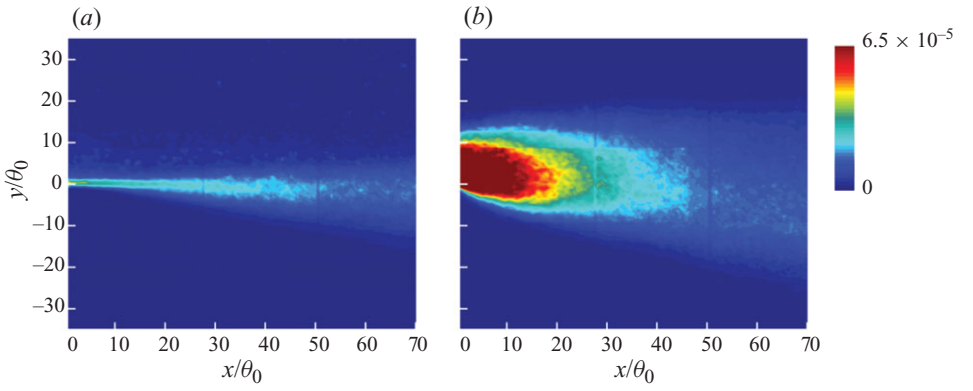


FIGURE 17. (Colour online) Raster plots of the estimated TKE dissipation rate $\varepsilon \cdot \theta_0/U_0^3$ for the baseline flow (*a*), and in the presence of actuation at $St = 0.05$ and $R_\mu = 0.63$ (*b*).

The work of Tanaka & Eaton (2007) demonstrated that estimates of the TKE dissipation rate from two-dimensional PIV measurements depend strongly on the spatial resolution. These authors noted that when the PIV vector spacing is larger than the Kolmogorov scale η, ε is underestimated, due to the inherent filtering of the fine scales. On the other hand, if the spacing is smaller than η, the error rapidly increases with the decrease in the spacing due to the increase in measurement noise. Based on the present spatial resolution and η, it is estimated that the vector spacing is about the same as the Kolmogorov scale, and therefore no significant errors due to noise are introduced. Based on the results of Tanaka & Eaton (2007), the calculated ε underestimates the TKE dissipation by about 20 % owing to resolution limitations. Figure 17 shows raster plots of the estimated TKE dissipation rates for the unforced and forced flows. In the absence of actuation (figure 17*a*), the dissipation is clearly confined to the centre segment of the shear layer. In the presence of actuation (applied upstream of the step edge) there is a nearly eight-fold increase in the magnitude of the measured dissipation immediately downstream of the step (figure 17*b*) and in its spatial extent relative to the baseline flow. The increased dissipation rate is more pronounced along the high-speed side of the shear layer than on the low-speed side, as a direct consequence of the advection of the small-scale vortices into the shear layer. As the flow evolves farther downstream, the absolute magnitude of ε decreases and eventually approaches the magnitude of the base flow. At the same time, the domain of increased dissipation spreads in the cross-stream direction and becomes more pronounced along the low-speed edge, and the peak in ε is displaced towards the low-speed side.

Distributions of integrated TKE across the shear layer in the absence and presence of actuation are shown in figure 18(*a*). As expected, in the presence of actuation the total energy k across the shear layer downstream of the step is larger than in the base flow and the increase is proportional to R_μ. However, the effect of the actuation diminishes farther downstream. For the intermediate actuation level, the curves for the baseline and actuated flows coincide for $x/\theta_0 > 70$, while at the high actuation level, k approaches the base level by $x/\theta_0 \approx 280$. While at the lowest actuation level the changes in the mean flow are minute, it actually results in lower k than in the base flow throughout the measurement domain (for $x/\theta_0 > 20$). Since the forced flows at intermediate and high R_μ are significantly wider than the baseline (cf. figure 11), the TKE levels within the forced flow are actually significantly lower than in the unforced flow. Alternatively, if the characteristic length scale in figure 18(*a*) is changed from

https://doi.org/10.1017/S0022112010001023 Published online by Cambridge University Press

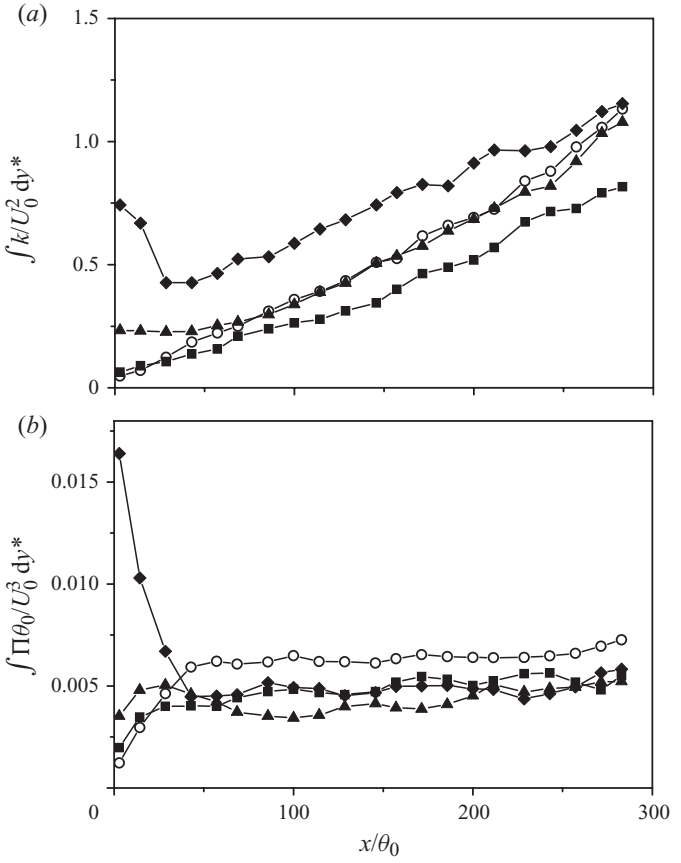


FIGURE 18. Streamwise evolution of the cross-stream integrated TKE k^* (*a*) and TKE production Π^* (*b*) for the baseline flow (○) and in the presence of actuation at $St = 0.05$ and $R_\mu = 0.06$ (■), 0.35 (▲) and 0.63 (◆).

θ_0 to the local θ, the dimensionless k falls below the baseline level regardless of the actuation level.

The effect of the actuation on turbulent production

$$\Pi = -\overline{uu}\frac{\partial \bar{U}}{\partial x} - \overline{vv}\frac{\partial \bar{V}}{\partial y} - \overline{uv}\left(\frac{\partial \bar{U}}{\partial y} + \frac{\partial \bar{V}}{\partial x}\right) \tag{5.2}$$

is assessed from integration of Π across the entire shear layer (figure 18*b*). In the absence of actuation, Π increases monotonically up to $x/\theta_0 = 60$ and thereafter is nearly invariant with x. At the low actuation level, there is a weak increase in Π through $x/\theta_0 < 20$ which is followed by a significant suppression of overall production throughout the measurement domain. At the intermediate actuation level there is a more pronounced and slightly longer domain of increased Π ($x/\theta_0 < 35$) which is followed by a second domain in which the production falls below the level of the baseline. Finally, even in the presence of high actuation level, in spite of a large initial increase in Π, the turbulence production within the shear layer falls below that of the base flow, beginning as far upstream as $x/\theta_0 \approx 40$. It is important to note that this upstream increase in production of TKE coincides with the significant enhancement of dissipation ε (cf. figure 17), and that these two coupled effects dominate the

https://doi.org/10.1017/S0022112010001023 Published online by Cambridge University Press

upstream development of the forced shear layer, marking enhanced dissipation of energy from the mean flow by the induced small-scale motions. Similarly, Dandois *et al.* (2007) also reported that high-frequency actuation led to a significant decrease in turbulent production (by about 30 %) over the base level.

The present results indicate that the actuation-induced closely coupled and strongly enhanced turbulent energy production and dissipation rate prematurely drain energy from the mean flow, and thereby lead to its stabilization to low-frequency perturbations. The spatial extent of the stabilized domain depends on the momentum flux ratio of the actuation. At low actuation levels the actuation vortex train is advected into the forming shear layer and therefore the stabilized domain commences closer to the shear layer origin. However, at higher actuation levels, the actuation vortices affect the shear layer farther downstream and therefore extend the streamwise stabilized domain.

6. Concluding remarks

The near-field evolution of small- and large-scale motions in a turbulent shear layer that forms downstream of a backward-facing step is altered by direct small-scale actuation that is effected within the boundary layer over the step surface. The actuation is applied using surface-integrated synthetic jets operating at frequencies that are significantly higher than the most unstable frequencies of the base flow, and within the dissipation range of the emerging shear layer. The actuation induces time-periodic modulation of the vorticity flux within the boundary layer, which is the primary source of vorticity for the separated shear layer, by the formation and advection of a train of discrete vortices having a characteristic cross-stream scale and streamwise spacing that are typically smaller than the boundary layer thickness. At low actuation levels, the vortex train is advected into the forming shear layer while at higher actuation amplitudes the train interacts with the shear layer along its high-speed edge with significant impact on the layer's cross-stream spreading and entrainment. The range of the interaction domain can be varied with the momentum flux of the actuation jet. The alteration of the base flow as a result of the actuation is captured by detailed, high-resolution velocity measurements in the cross-stream plane of the flow using phase- and ensemble-averaged PIV and single-sensor hot-wire anemometry.

The present work demonstrated that small-scale actuation has a profound effect on the evolution of both the large- and small-scale motions within the near field of the shear layer. Stability considerations show that when the actuation frequency is higher than about twice the highest 'natural' frequency along the shear layer (i.e. when $\omega > 2\omega_{n,0}$), the 'natural' near-field evolution of the layer is suppressed. Actuation at finite levels can be characterized by nonlinear interactions between the high-frequency, low-frequency and the global modes of the flow. It results in reduced receptivity to low-frequency disturbances, and in decrease of energy transfer and feedback effects of the flow's global mode. Spectral measurements show that even though the actuation is applied at a single frequency, there is a broadband increase in the energy of the small-scale motions that is accompanied by a decrease in the energy of the large-scale motions. These large scales are typically associated with the 'most amplified', unstable modes of the base flow. The energy reduction of these motions is the result of both increased entrainment and mixing of high- and low-speed fluid that is manifested by increased cross-stream spreading, and simultaneous increases in the mean cross-stream width and in turbulent production.

https://doi.org/10.1017/S0022112010001023 Published online by Cambridge University Press

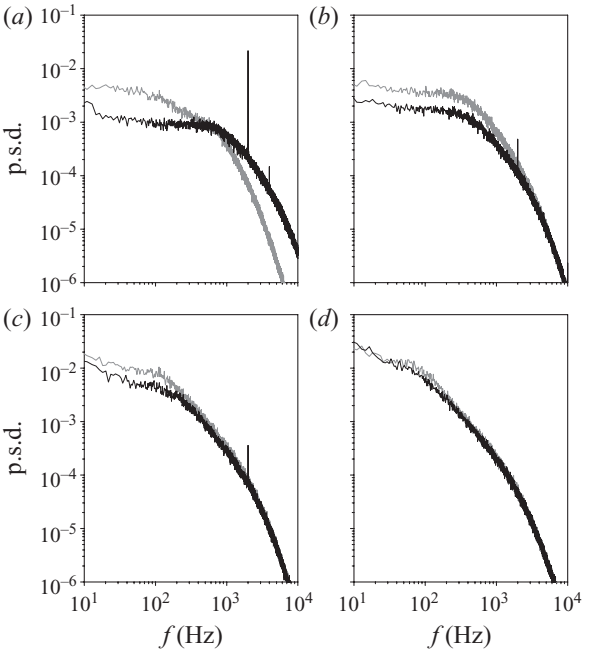


FIGURE 19. Power spectra of velocity fluctuations for the absence (grey) and presence (black) of actuation at $St = 0.05$ and $R_\mu = 0.35$ at $y|_{0.5U_0}$ and $x/\theta_0 = 14.5$ (*a*), 58 (*b*), 203.2 (c) and 348.3 (*d*).

The near field of the forced shear layer has three distinct domains. The first domain (D-1), immediately downstream of the step edge ($x/\theta_0 < 50$), is dominated by significant concomitant increases in the production of the TKE and its cross-stream integral (figures 18*a* and 18*b*), the cross-stream width of the shear layer (figure 11), and in the dissipation of TKE (figure 17*b*). In the second streamwise domain (D-2), the streamwise rates of change of these quantities become similar to the corresponding rates in the unforced flow (e.g. $\theta(x)$ in figure 11 and $TKE(x)$ in figure 18*a*) although their magnitudes are substantially different. For example, as noted in connection with the discussion of figure 18, the turbulent production in the forced flow is lower than the production in the unforced flow, and, depending on the actuation level, $TKE(x)$ in D-2 is either below ($R_\mu = 0.06$) or above ($R_\mu = 0.35$, 0.63) the corresponding levels of the baseline flow indicating a mismatch between production and dissipation in D-2.

That the streamwise rates of change of these quantities are similar to the corresponding rates in the unforced flow, suggests that the effects of the actuation in D-2 are diminished to the point where the shear layer begins to resume its characteristic 'natural' streamwise evolution. However, what primarily characterizes the forced flow in this domain is the evolution of its spectral content. An example is shown in figure 19 which includes power spectra of the baseline and forced flows ($St_{\theta 0} = 0.05$ and $R_\mu = 0.35$) at four streamwise stations ($x/\theta_0 = 14.5$, 58, 203.2 and 348.3). These spectra are taken at cross-stream elevations where the streamwise velocity is $U_0/2$. While in D-1 ($x/\theta_0 = 14.5$), there is a significant increase in the small-scale motions (as may be expected from the increase in production in figure 18*b*), there is also a significant reduction in the magnitude of the spectral components that correspond to the large-scale motions. Within D-2, the magnitudes of the spectral components at the small scales (high frequencies) begin to coincide with the magnitudes of the

https://doi.org/10.1017/S0022112010001023 Published online by Cambridge University Press

corresponding spectral components in the baseline flow indicating that dissipation outpaces production. It is noteworthy that although the cross-stream extent of the forced flow is larger than in the baseline, the comparable streamwise growth rate of the two flows suggests that entrainment is similar. The data in figure 11 indicate that in the presence of strong actuation ($R_\mu = 0.63$) the streamwise growth rate decreases somewhat when the actuation vortex train merges with the high-speed edge of the layer.

The second feature of the spectra in figure 19(*b*, *c*) is the lower magnitude of the spectral components that correspond to large-scale motions compared to the baseline flow. This effect persists through the entire domain D-2 (up to about $x/\theta_0 = 350$) where the two spectra become almost indistinguishable. These data indicate that within D-2 the spectral components corresponding to the frequencies associated with the large-scale motion remain suppressed and amplify slowly. In fact, figure 13 shows that the actuation results in significant attenuation of spectral components up to 300 Hz, while figure 12 shows the streamwise reduction in the magnitude of the most amplified frequency. Therefore, it may be concluded that while amplification of unstable modes in the forced shear layer resumes in D-2, the most amplified modes that emerge at the downstream end of D-2 have significantly lower frequencies than the unforced flow would have at the same streamwise position. The mechanisms of shear layer stabilization proposed by Stanek *et al.* (2002) are in accord with the structural modification of the shear layer within D-2.

Finally, in the third domain (D-3), the inviscid instability of the shear layer resumes in what might be described as a 'new' baseline flow but, as noted above, with significantly lower unstable frequencies than the unforced flow would have had at the same streamwise position (in the present flow, this domain nominally extends beyond $x/\theta_0 \approx 350$).

Appendix. A reduced-order model

Consider a two-dimensional unsteady incompressible flow of Newtonian fluid around a backward facing step of height H with far-field speed U_0 (see figure 3*a*). The axial and vertical distances from the step corner are scaled with H, time is scaled with H/U_0, and the velocity components are scaled with U_0. The flow motion is described by the Navier–Stokes equations in the non-dimensional vorticity and stream function formulation:

$$\left.\begin{aligned} &\chi_t + \psi_y \chi_x - \psi_x \chi_y = Re(\chi_{xx} + \chi_{yy})/2, \\ &\chi = -(\psi_{xx} + \psi_{yy}). \end{aligned}\right\} \tag{A 1}$$

Here $\psi(x, y, t)$ is the stream function and $\chi(x, y, t)$ is the vorticity. The flow axial and transverse velocity components are given by $u = \psi_y$, $v = -\psi_x$ and $Re = \rho U_0 H/\mu$, where ρ and μ are the flow constant density and viscosity.

The flow is subjected to the following boundary conditions. Along the inlet section at $x = 0$ and $y > 0$ the incoming stream function and the vorticity are prescribed for $t > 0$ as follows:

$$\left.\begin{aligned} &\psi(0, y, t) = \psi_0(y) + \kappa g(y, t), \\ &\chi(0, y, t) = -\psi_{0yy} - \kappa g_{yy}(y, t). \end{aligned}\right\} \tag{A 2}$$

Here, $\psi_0(y)$ describes the inlet base volumetric flux, resulting in a base incoming axial velocity profile $U(y) = \psi_{0y}(y)$, representing a boundary layer, where U is zero at $y = 0$ and tends to one as y increases. This base velocity profile is perturbed by a

https://doi.org/10.1017/S0022112010001023 Published online by Cambridge University Press

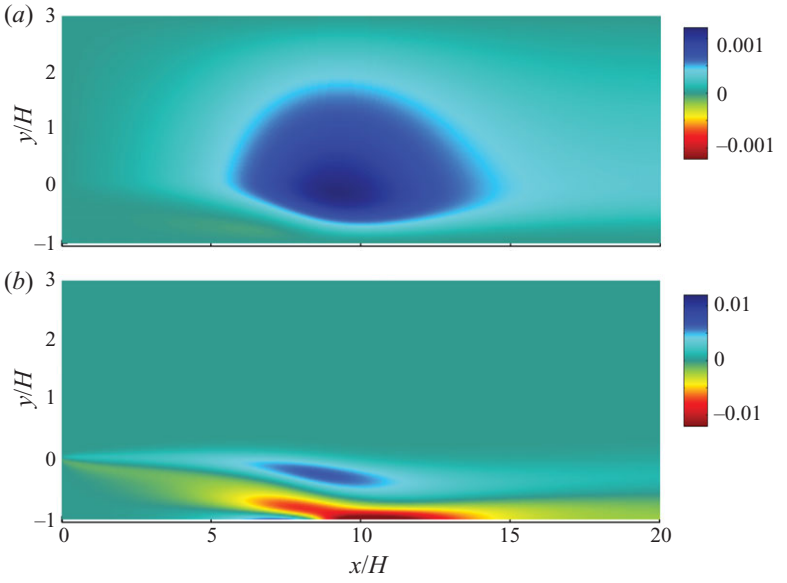


FIGURE 20. (Colour online) The perturbation functions of the global mode ψ_g (*a*) and χ_g (*b*) at $Re = 1000$.

perturbation flux of given characteristic level κ and shape, $g(y, t)$ representing a train of incoming vortices within the boundary layer, where typically $0 \leqslant \kappa \ll 1$, $g(0, t) = 0$, and g tends to zero as y increases. Along the step walls the no penetration and no slip conditions are set, i.e. for all time $t > 0$:

$$\left.\begin{aligned} &\text{For } -1 \leqslant y < 0 : \psi(0, y, t) = \psi_x(0, y, t) = 0, \\ &\text{For } 0 \leqslant x \leqslant \infty : \psi(x, -1, t) = \psi_y(x, -1, t) = 0. \end{aligned}\right\} \tag{A 3}$$

As $y \to \infty$ it is assumed that the transverse velocity approaches zero, i.e. for all time $t > 0$:

$$\psi_x(x, y \to \infty, t) = 0. \tag{A 4}$$

Also, as $x \to \infty$, the transverse velocity and vorticity axial gradient approach zero for all time $t > 0$:

$$\psi_x(x, y, t) = \chi_x(x, y, t) = 0. \tag{A 5}$$

The direct numerical simulation code of Hawa & Rusak (2001) is used to establish a base state solution $\Psi(x, y)$ of (A 1)–(A 5) at a fixed Re, with an inlet axial velocity profile $U(y) = \tanh(y/\beta)$ and with no upstream excitation, i.e. $\kappa = 0$ for all time t. Moreover, the unsteady simulations also show that as the non-actuated flow asymptotically converges in time to the steady state $\Psi(x, y)$, it is characterized by a global mode of exponential decay in time, i.e. for a sufficiently large t

$$\psi(x, y, t) = \Psi(x, y) + \exp(-\sigma t)\psi_g(x, y). \tag{A 6}$$

For example, the computations show that at $Re = 1000$ and with $\beta = 0.03$ the decay rate $\sigma = 0.014$ and the global mode perturbation stream function ψ_g and related vorticity χ_g are centred near the reattachment point at $x \sim 10H$, where the shear layer transitions into a wall boundary layer, and decay with distance from this point (figure 20).

https://doi.org/10.1017/S0022112010001023 Published online by Cambridge University Press

For a high Re flow, the shear layer of the baseline backward-facing step flow develops over a longer streamwise transverse distance, typically of the order of the separation zone length $l_s \gg H$. Let $\varepsilon = H/l_s \ll 1$. The axial distance is rescaled so that $\tilde{x} = \varepsilon x$. Then, the base steady flow solution of (A 1)–(A 5) is described by the stream function: $\Psi = \Psi(\tilde{x}, y; Re)$. The base axial velocity is given by $u = \Psi_y(\tilde{x}, y; Re)$ and vertical velocity is $v = -\varepsilon\Psi_{\tilde{x}}(\tilde{x}, y; Re)$.

Following the asymptotic multi-scale linear stability analysis of Rusak & Eisle (2005) for sufficiently small ε and κ, it can be shown that when the upstream excitation is characterized by a non-dimensional (real) frequency ω, the perturbed flow stream function ψ may be composed of the base flow stream function $\Psi(\tilde{x}, y; Re)$, a perturbation ψ_1 of the shear layer response to the excitation as if it is a free layer (the forced behaviour), and the global mode of the non-actuated flow ψ_g (the homogeneous behaviour), i.e.

$$\psi(x, y, t; \delta, Re, \omega) = \Psi(\tilde{x}, y; Re) + \kappa\psi_1(x, \tilde{x}, y, t; Re, \omega) + \gamma(t)\psi_g(\tilde{x}, y; Re) + O(\varepsilon^2, \kappa^2, \varepsilon\kappa, \gamma^2, \varepsilon\gamma, \kappa\gamma). \quad \text{(A 7)}$$

Here, the perturbation function ψ_1 is given in terms of the regular scale x and the long scale $\tilde{x}$ by

$$\psi_1(x, \tilde{x}, y, t; Re, \omega) = A(\tilde{x}; Re, \omega) \exp\left[\int_0^x \alpha_I(\tilde{x}'; Re, \omega)\,\mathrm{d}\tilde{x}'\right] \times \sqrt{\phi_R^2(\tilde{x}, y; Re, \omega) + \phi_I^2(\tilde{x}, y; Re, \omega)} \sin\left(\omega t - \int_0^x \alpha_R(\tilde{x}'; Re, \omega)\,\mathrm{d}\tilde{x}' + \varphi(\tilde{x}; Re, \omega)\right). \quad \text{(A 8)}$$

The first and third terms in (A 8) describe a slower change of the perturbation with distance, whereas the integral terms in (A 8) describe the perturbations growth rate and periodicity over a regular scale. For a given frequency ω, the complex eigenfunction $\phi = \phi_R + \mathrm{i}\phi_I$ and the complex wavenumber $\alpha = \alpha_R + \mathrm{i}\alpha_I$ are determined from the eigenvalue problem of the linear spatial stability analysis:

$$\left.\begin{aligned} L(\phi) = (\Psi_y(\tilde{x}, y; Re)\alpha - \omega)(\phi_{yy} - \alpha^2\phi) - \alpha\Psi_{yyy}(\tilde{x}, y; Re)\phi \\ + \frac{\mathrm{i}}{Re}(\phi_{yyyy} - 2\alpha^2\phi_{yy} + \alpha^4\phi) = 0, \\ \phi(y = -1, x) = 0 \text{ and as } y \to \infty,\ \phi \to 0. \end{aligned}\right\} \quad \text{(A 9)}$$

The function $A(\tilde{x}; \omega)$ in (A 8) is described by the equation

$$A_{\tilde{x}} + q(\tilde{x}; \omega)A = 0. \quad \text{(A 10)}$$

Here $q(\tilde{x}; \omega) = \int_{-1}^{\infty} b\bar{\phi}\,\mathrm{d}y / \int_{-1}^{\infty} a\bar{\phi}\,\mathrm{d}y$, $\bar{\phi}$ is the complex conjugate of ϕ, and

$$a = 2\omega\alpha\phi + \Psi_y(\phi_{yy} - 3\alpha^2\phi) - \Psi_{yyy}\phi,$$
$$b = \omega(\alpha_{\tilde{x}}\phi + 2\alpha\phi_{\tilde{x}}) + \Psi_y(\phi_{yy\tilde{x}} - 3\alpha^2\phi_{\tilde{x}} - 3\alpha\alpha_{\tilde{x}}\phi) - \Psi_{yyy}\phi_{\tilde{x}} - \Psi_{\tilde{x}}(\phi_{yyy} - \alpha^2\phi_y) + \Psi_{yy\tilde{x}}\phi_y.$$

The solution of (A 10) shows that A behaves like

$$A(\tilde{x}; \omega) = \exp\left[-\int_0^{\tilde{x}} q(\tilde{x}'; \omega)\,\mathrm{d}\tilde{x}'\right]. \quad \text{(A 11)}$$

Note that the amplitude $\gamma(t)$ of the global mode is excited by the magnitude of the perturbation $\kappa\psi_1$ at some distance away from the step section, but cannot be

https://doi.org/10.1017/S0022112010001023 Published online by Cambridge University Press

determined by a linear analysis. The nonlinear analysis is the subject of a follow-on paper.

This research was supported by the FLOWCAD Programme of Air Force Research Laboratory at Wright–Patterson AFB, and by the Boeing Company. The authors thank Dr Michael Stanek for suggesting the concept of a single, 'broadband' shear layer stability analysis, and for a number of insightful discussions during the course of this investigation. The authors are also grateful to Mr David Lucas for his assistance during parts of the experimental work.

REFERENCES

Arunajatesan, S., Shipman, J. D. & Sinha, N. 2002 Hybrid RANS-LES simulation of cavity flow fields with control. *Paper 2002–1130*. AIAA.

Ben-Hamou, E., Arad, E. & Seifert, A. 2007 Generic transport aft-body drag reduction using active flow control. *Flow Turbul. Combust*. **78**, 365–382.

Bower, W. W., Kibens, V., Cary, A. W., Alvi, F. S., Raman, G., Annaswamy, A. & Malmuth, N. M. 2004 High-frequency excitation active flow control for high-speed weapon release (HIFEX). *Paper 2004–2513*. AIAA.

Brown, G. L. & Roshko, A. 1974 On density effects and large structure in turbulent mixing layers. *J. Fluid Mech.* **64**, 775–816.

Cain, A. B., Rogers, M. M., Kibens, V. & Raman, G. 2001 Simulations of high-frequency excitation of a plane wake. *Paper 2001–0514*. AIAA.

Cattafesta, L. N., Song, Q., Williams, D. R., Rowley, C. W. & Alvi, F. S. 2008 Active control of flow-induced cavity oscillations. *Prog. Aerosp. Sci.* **44**, 479–502.

Dandois, J., Garnier, E. & Sagaut, P. 2007 Numerical simulation of active separation control by a synthetic jet. *J. Fluid Mech.* **574**, 25–58.

Debiasi, M. & Samimy, M. 2003 An experimental study of the cavity flow for closed-loop flow control. *Paper 2003–4003*. AIAA.

Erk, P. P. 1997 Separation control on a post-stall airfoil using acoustically generated perturbations. PhD dissertation, Hermann-Föttinger-Institut für Strömungsmechanik, Technische Universität Berlin.

Glezer, A., Amitay, M. & Honohan, A. M. 2005 Aspects of low- and high-frequency actuation for aerodynamic flow control. *AIAA J.* **43**, 1501–1511.

Greenblatt, D. & Wygnanski, I. J. 2000 The control of flow separation by periodic excitation. *Prog. Aerosp. Sci.* **36**, 487–545.

Gutmark, E. J., Schadow, K. C. & Yu, K. H. 1995 Mixing enhancement in supersonic free shear flows. *Annu. Rev. Fluid Mech.* **27**, 375–417.

Hawa, T. & Rusak, Z. 2001 The dynamics of a laminar flow in a symmetric channel with a sudden expansion. *J. Fluid Mech.* **436**, 283–320.

Ho, C.-M. & Huerre, P. 1984 Perturbed free shear layers. *Annu. Rev. Fluid Mech.* **16**, 365–424.

Honohan, A. M., Amitay, M. & Glezer, A. 2000 Aerodynamic control using synthetic jets. *Paper 2000–2401*. AIAA.

Hussain, A. K. M. F. & Hasan, M. A. Z. 1985 Turbulence suppression in free turbulent shear flows under controlled excitation. Part 2. Jet-noise reduction. *J. Fluid Mech.* **150**, 159–168.

Lucas, D. G. 2005 High frequency direct excitation of small-scale motions in planar shear flows. MS thesis, Georgia Institute of Technology, Atlanta, GA.

Michalke, A. 1964 On the inviscid instability of the hyperbolictangent velocity profile. *J. Fluid Mech.* **19** (4), 543–556.

Morris, S. C. & Foss, J. F. 2003 Turbulent boundary layer to single-stream shear layer: the transition region. *J. Fluid Mech.* **494**, 187–221.

Nallasamy, M. & Hussain, A. K. M. F. 1989 Effects of excitation on turbulence levels in a shear layer. *Trans. ASME J. Fluids Engng* **111**, 102–104.

Oljaca, M. & Glezer, A. 2009 The effects of induced dissipative small-scale motions and mixing on optical distortion in a plane shear layer. *J. Fluid Mech.* **619**, 295–329.

https://doi.org/10.1017/S0022112010001023 Published online by Cambridge University Press

Roberts, F. A. & Roshko, A. 1985 Effects of a periodic forcing on mixing in turbulent shear layers and wakes. *Paper 85–0570*. AIAA.

Rockwell, D. O. 1972 External excitation of planar jets. *Trans. ASME J. Appl. Mech.* **39**, 883–890.

Rockwell, D. & Naudascher, E. 1978 Review: self-sustaining oscillations of flow past cavities. *Trans.* ASME *J. Fluids Engng* **100**, 152–165.

Rusak, Z. & Eisele, I. 2005 Controlled manipulation of small and large scales in a turbulent shear layer. Part II. Stability studies. *Paper 2005–4754*. AIAA.

Samimy, M., Kim, J.-H., Kastner, J., Adamovich, I. & Utkin, Y. 2007 Active control of a Mach 0.9 jet for noise mitigation using plasma actuators. *AIAA J.* **45**, 890–901.

Shaw, L. L., Smith, B. R. & Saddoughi, S. 2006 Full-scale flight demonstration of active control of a pod wake. *Paper 2006–3185*. AIAA.

Smith, B. L. & Glezer, A. 1998 The formation and evolution of synthetic jets. *Phys. Fluids* **10**, 2281–2297.

Stanek, M. J., Raman, G., Kibens, V., Ross, J. A., Odedra, J. & Peto, J. 2000 Control of cavity resonance through very high frequency forcing. *Paper 2000–1905*. AIAA.

Stanek, M. J., Raman, G., Ross, J. A., Odedra, J., Peto J., Alvi, F. & Kibens, V. 2002 High frequency acoustic suppression: the role of mass flow, the notion of superposition, and the role of inviscid instability – a new model (Part II). *Paper 2002–2404*. AIAA.

Stanek, M. J., Visbal, M. R., Rizzetta, D. P., Rubin, S. G. & Khosla, P. K. 2007 On a mechanism of stabilizing turbulent free shear layers in cavity flows. *Comput. Fluids* **36**, 1621–1637.

Tanaka, T. & Eaton, J. K. 2007 A correction method for measuring turbulence kinetic energy dissipation rate by PIV. *Exp. Fluids* **42**, 893–902.

Unal, M. F. & Rockwell, D. 1988 On vortex formation from a cylinder. Part 1. The initial instability. *J. Fluid Mech.* **190**, 491–512.

Visbal, M. & Rizzetta, D. 2008 Effect of flow excitation on aero-optical aberration. *Paper 2008–1074*. AIAA.

Vlasov, E. V. & Ginevskii, A. S. 1973 Generation and suppression of turbulence in an axisymmetric turbulent jet under an acoustic effect. *J. Fluid Dyn.* **8**, 881–885.

Vukasinovic, B. & Glezer, A. 2006 Transitory fluidic control of turbulent shear flows. *Paper 2006–3227*. AIAA.

Vukasinovic, B. & Glezer, A. 2007 Control of a separating flow over a turret. *Paper 2007–4506*. AIAA.

Vukasinovic, B., Glezer, A., Gordeyev, S., Jumper, E. & Kibens, V. 2009 Fluidic control of a turret wake. Part I. Aerodynamic effects. *Paper 2009–816*. AIAA.

Vukasinovic, B., Lucas, D. G. & Glezer, A. 2004 Direct manipulation of small-scale motions in a plane shear layer. *Paper 2004–2617*. AIAA.

Vukasinovic, B., Lucas, D. G. & Glezer, A. 2005 Controlled manipulation of small- and large-scales in a turbulent shear layer. Part I. Experimental studies. *Paper 2005–4753*. AIAA.

Wiltse, J. M. & Glezer, A. 1993 Manipulation of free shear flows using piezoelectric actuators. *J. Fluid Mech.* **249**, 261–285.

Wiltse, J. M. & Glezer, A. 1998 Direct excitation of small scale motions in free shear flows. *Phys. Fluids* **8**, 2026–2036.

Winant, C. D. & Browand, F. K. 1974 Vortex pairing, the mechanism of turbulent mixing layer growth at moderate Reynolds number. *J. Fluid Mech.* **63**, 237–255.

Wu, J.-Z., Lu, X.-Y., Denny, A. G., Fan, M. & Wu, J.-M. 1998 Post-stall flow control on an airfoil by local unsteady forcing. *J. Fluid Mech.* **371**, 21–58.

Zaman, K. B. M. Q. & Hussain, A. K. M. F. 1981 Turbulence suppression in free shear flows by controlled excitation. *J. Fluid Mech.* **103**, 133–159.

Zaman, K. B. M. Q. & Rice, E. J. 1992 On the mechanism of turbulence suppression in free shear flows under acoustic excitation. *Tech. Memo*. 105360. NASA.

Zubair, F. R., Freeman, A. P., Piatrovich, S., Shockro, J., Ibrahim, Y. N. & Catrakis, H. J. 2007 Large scale turbulence suppression control for direct reduction of aero-optical aberrations. *Paper 2007–4008*. AIAA.

https://doi.org/10.1017/S0022112010001023 Published online by Cambridge University Press